

Constraining M_ν with the Bispectrum I: Breaking Parameter Degeneracies

CHANGHOON HAHN,^{1,2,*} FRANCISCO VILLAESCUSA-NAVARRO,³ EMANUELE CASTORINA,^{2,1} AND
ROMAN SCOCCIMARRO⁴

¹*Lawrence Berkeley National Laboratory, 1 Cyclotron Rd, Berkeley CA 94720, USA*

²*Berkeley Center for Cosmological Physics, University of California, Berkeley, CA 94720, USA*

³*Center for Computational Astrophysics, Flatiron Institute, 162 5th Avenue, New York, NY 10010, USA*

⁴*Center for Cosmology and Particle Physics, Department of Physics, New York University, NY 10003, New York, USA*

(Dated: DRAFT --- 9b87e2a --- 2019-06-14 --- NOT READY FOR DISTRIBUTION)

ABSTRACT

Massive neutrinos suppress the growth of structure below their free-streaming scale and leave an imprint on large-scale structure. Measuring this imprint allows us to constrain the sum of neutrino masses, M_ν , a key ingredient for particle physics beyond the Standard Model. However, degeneracies with cosmological parameters limit the constraining power of standard two-point clustering statistics. In this work, we investigate whether we can break these parameter degeneracies and constrain M_ν with the next higher-order correlation function, the bispectrum. We first examine the degeneracy between M_ν and σ_8 using 800 N -body simulations from the HADES suite and demonstrate that the redshift-space halo bispectrum helps break this degeneracy. Next, we quantify the information content of the redshift-space halo bispectrum in a Fisher matrix forecast that includes M_ν and cosmological parameters Ω_m , Ω_b , h , n_s , and σ_8 . This is the first N -body simulation based Fisher matrix forecast of cosmological parameters using the bispectrum. More importantly, for $k_{\text{max}} = 0.2$ and 0.5 we find

Keywords: cosmology: —

1. INTRODUCTION

The lower bound on the sum of neutrino masses ($M_\nu \gtrsim 0.06$ eV), discovered by neutrino oscillation experiments, provides strong evidence of physics beyond the Standard Model of particle physics (Forero et al. 2014; Gonzalez-Garcia et al. 2016). A more precise measurement of M_ν has the potential to distinguish between the ‘normal’ and ‘inverted’ neutrino mass hierarchy scenarios and further reveal the physics of neutrinos. Neutrino oscillation experiments, however, are insensitive to the absolute neutrino mass scales. Other laboratory experiments sensitive to M_ν (e.g. double beta decay and tritium beta decay experiments) have the potential to place upper bounds of $M_\nu < 0.2$ eV

* hahn.changhoon@gmail.com

in upcoming experiments (Drexlin et al. 2013, CH: hmm, who do I cite). These upper bound alone are not insufficient to distinguish between the mass hierarchies. Neutrinos through the cosmic neutrino background affect the expansion history and the growth of cosmic structure. Measuring these effects with cosmological observables provides complementary and potentially more precise measurements of M_ν .

Neutrinos, in the early universe, are relativistic and contribute to the energy density of radiation. Later as they become non-relativistic, they contribute to the energy density of matter. This transition affects the expansion history of the universe and leaves imprints observable in the cosmic microwave background (CMB) anisotropy spectrum (citecitecite). Massive neutrinos also impact the growth of structure. On large scales, neutrino perturbations are indistinguishable from perturbations of cold dark matter (CDM). However, on scales smaller than their free-streaming scale, neutrinos do not contribute the clustering and thereby reduce the total matter power spectrum. In addition, they also reduce the growth rate of CDM perturbations at late times. This combined suppression of the small-scale matter power spectrum also leaves measurable imprints on the CMB as well as large-scale structure. For more details the effect of neutrinos in cosmological observables, we refer readers to Lesgourgues & Pastor (2012, 2014); Gerbino (2018).

The tightest cosmological constraints on M_ν currently come from combining CMB data with other cosmological probes. Temperature and large angle polarization data from the *Planck* satellite places an upper bound of $M_\nu < 0.54$ eV with 95% confidence level (Collaboration et al. 2018b). Adding the Baryon Acoustic Oscillation (BAO) to the *Planck* likelihood breaks geometrical degeneracies (M_ν , h , Ω_m) and significantly tightens the upper bound to $M_\nu < 0.16$ eV. CMB lensing further tightens the bound further to $M_\nu < 0.13$ eV, though not as significantly. Combining these probes, however, introduce a strong correlation between M_ν and A_s , the scale amplitude. Since CMB experiments measure the combined quantity $A_s e^{-2\tau}$, where τ is the optical depth of reionization, this leads to a strong degeneracy between M_ν and τ (Allison et al. 2015; Liu et al. 2016; Archidiacono et al. 2017).

The $\tau - M_\nu$ degeneracy will continue to be a major bottleneck for M_ν constraints from CMB data. The best constraints on τ currently come from *Planck* ($\tau \sim 0.06$). However, upcoming ground-based CMB experiments (*e.g.* CMB-S4) will not observe scales larger than $\ell < 30$, and therefore will not directly constrain τ (Abazajian et al. 2016). Meanwhile, proposed future space-based experiments such as LiteBIRD¹ and CoRE², which have the potential to precisely measure τ , have yet to be confirmed. CMB data, however, is not the only way to improve M_ν constraints. The imprint of neutrinos on 3D clustering can be measured to constrain M_ν and with the sheer cosmic volumes mapped by upcoming surveys, *e.g.* DESI³, PFS⁴, EUCLID⁵, and WFIRST⁶, will be able tightly constrain M_ν (Audren et al. 2013; Font-Ribera et al. 2014; Petracca et al. 2016; Sartoris et al. 2016; Boyle & Komatsu 2018).

¹ <http://litebird.jp/eng/>

² <http://www.core-mission.org/>

³ <https://www.desi.lbl.gov/>

⁴ <https://pfs.ipmu.jp/>

⁵ <http://sci.esa.int/euclid/>

⁶ <https://wfirst.gsfc.nasa.gov/>

A major limitation of using 3D clustering is modeling beyond linear scales, for bias tracers, and in redshift space. Simulations have made huge strides in accurately and efficiently modeling nonlinear structure formation with massive neutrinos (*e.g.* Brandbyge et al. 2008; Villaescusa-Navarro et al. 2013; Castorina et al. 2015; Adamek et al. 2017; Emberson et al. 2017; Villaescusa-Navarro et al. 2018). In conjunction, new simulation based ‘emulation’ models that exploit the accuracy of N -body simulations while minimizing the computing budget have been applied to analyze small-scale galaxy clustering with remarkable success (*e.g.* Heitmann et al. 2009; Kwan et al. 2015; Collaboration et al. 2018a; McClintock et al. 2018; Zhai et al. 2018; Wibking et al. 2019). Developments on these fronts have the potential to unlock the information content in nonlinear clustering to constrain M_ν .

Various works have examined the impact of neutrino masses on nonlinear clustering of matter in real-space (*e.g.* Saito et al. 2008; Wong 2008; Saito et al. 2009; Viel et al. 2010; Agarwal & Feldman 2011, **CH: add more citations**) and in redshift-space (Marulli et al. 2011; Castorina et al. 2015; Upadhye et al. 2016). Most recently, using a suite of more than 1000 simulations, Villaescusa-Navarro et al. (2018) examined the impact of M_ν on the redshift-space matter and halo power spectrum to find the imprint of M_ν and σ_8 on the power spectrum are degenerate and differ only by $< 1\%$. The strong $M_\nu - \sigma_8$ degeneracy poses a serious limitation of constraining M_ν with the power spectrum. However, information in the nonlinear regime extend beyond the power spectrum to higher-order statistics— *e.g.* the bispectrum. In fact, the bispectrum has comparable a signal-to-noise ratio to the power spectrum on nonlinear scales (Sefusatti & Scoccimarro 2005; Chan & Blot 2017). Furthermore, although M_ν is not included in their analysis, Sefusatti et al. (2006) and Yankelevich & Porciani (2019) have shown that including the bispectrum in analyses improves constraints on cosmological parameters. Ruggeri et al. (2018) presented the first measurement of the bispectrum for N -body simulations with massive neutrinos. Yet, no work to date has quantified the full information content and constraining power of the bispectrum down to nonlinear scales — especially for M_ν .

In this work, we examine the effect of massive neutrinos on the redshift-space halo bispectrum using more than 23000 N -body simulations with massive neutrinos. We first demonstrate that the bispectrum helps break the M_ν - σ_8 degeneracy found in the power spectrum. Then we present the full information content of the bispectrum for all triangle configurations down to $k_{\text{max}} = 0.5 \, h/\text{Mpc}$ using a Fisher forecast where we estimate the covariance matrix and derivatives with the large set of simulations from the Quijote suite (Villaescusa-Navarro et al. in preparation). This paper is the first of a series of papers that aim to demonstrate the potential of the galaxy bispectrum analysis in constraining M_ν . In the subsequent paper, we will include HOD parameters in our forecasts to quantify the full information content of the galaxy bispectrum. In the series, we will also present methods to tackle challenges that come with analyzing the full galaxy bispectrum, such as data compression for reducing the dimensionality of the bispectrum.

In Section 2 we describe the two simulation suites, HADES and Quijote, that we use throughout the paper. Then in Section 3, we describe how we measure the bispectrum of these simulations. We then present in Section 4.1, using the redshift-space halo bispectrum of HADES simulations, how M_ν leaves a distinct imprint on the bispectrum which allows the bispectrum to break the degeneracy between M_ν and σ_8 . Finally, in Section 4.2 we present the full information content of the halo bispectrum

with a Fisher forecast of cosmological parameters using the Quijote simulations and demonstrate the how the bispectrum drastically improves the constraints on the cosmological parameters: Ω_m , Ω_b , h , n_s , σ_8 , and *especially* M_ν .

2. HADES AND QUIJOTE SIMULATION SUITES

The HADES⁷ and Quijote suites are sets of, 23000 total, N -body simulations run on multiple cosmologies, include those with massive neutrinos ($M_\nu > 0$ eV). In this work, we use a subset of the HADES and Quijote simulations. Below, we briefly describe these simulations; a brief summary of the simulations can be found in Table 1. The HADES simulations start from Zel’dovich approximated initial conditions generated at $z = 99$ using the Zennaro et al. (2017) rescaling method and follow the gravitational evolution of $N_{\text{cdm}} = 512^3$ CDM, plus $N_\nu = 512^3$ neutrino particles (for $M_\nu > 0$ eV cosmologies), to $z = 0$. They are run using the GADGET-III TreePM+SPH code (Springel 2005) in a periodic $(1 h^{-1}\text{Gpc})^3$ box. All of the HADES simulations share the following cosmological parameter values, which are in good agreement with Planck constraints Ade et al. (2016): $\Omega_m=0.3175$, $\Omega_b=0.049$, $\Omega_\Lambda=0.6825$, $n_s=0.9624$, $h=0.6711$, and $k_{\text{pivot}} = 0.05 h\text{Mpc}^{-1}$.

The HADES suite includes N -body simulations with degenerate massive neutrinos of $M_\nu = 0.06$, 0.10 , and 0.15 eV. These simulations are run using the “particle method”, where neutrinos are described as a collisionless and pressureless fluid and therefore modeled as particles, same as CDM (Brandbyge et al. 2008; Viel et al. 2010). HADES also includes simulations with massless neutrino and different values of σ_8 to examine the $M_\nu - -\sigma_8$ degeneracy. The σ_8 values were chosen to match either σ_8^m or $\sigma_8^c - \sigma_8$ computed with respect to total matter (CDM + baryons + ν) or CDM + baryons — of the massive neutrino simulations: $\sigma_8 = 0.822, 0.818, 0.807$, and 0.798 . Each model has 100 independent realizations and we focus on the snapshots saved at $z = 0$. Halos closely trace the CDM+baryon field rather than the total matter field and neutrinos have negligible contribution to halo masses (*e.g.* Ichiki & Takada 2012; Castorina et al. 2014; LoVerde 2014; Villaescusa-Navarro et al. 2014). Hence, dark matter halos are identified in each realization using the Friends-of-Friends algorithm (FoF; Davis et al. 1985) with linking length $b = 0.2$ on the CDM + baryon distribution: only halos with masses above $3.2 \times 10^{13} h^{-1} M_\odot$ are included. We refer readers to Villaescusa-Navarro et al. (2018) for more details on the HADES simulations.

In addition to HADES, we use simulations from the Quijote suite, a set of 23,000 N -body simulations that in total contain more than 3.3 trillion (3.3×10^{12}) particles over a volume of $23000(h^{-1}\text{Gpc})^3$. These simulations were constructed to quantify the information content of different cosmological observables using Fisher matrix forecasting (Section 4.2). They are therefore designed to accurately calculate the covariance matrices of observables and the derivatives of observables with respect to cosmological parameters. The suite considers 6 cosmological parameters: Ω_m , Ω_b , h , n_s , σ_8 , and M_ν .

To calculate covariance matrices, Quijote includes $N_{\text{cov}} = 15,000$ N -body simulations run at a fiducial cosmology ($\Omega_m=0.3175$, $\Omega_b=0.049$, $h=0.6711$, $n_s=0.9624$, $\sigma_8=0.834$, and $M_\nu=0.0$ eV). It also includes sets of 500 N -body simulations run at different cosmologies where only one parameter is varied from the fiducial cosmology at a time for the derivatives. Along Ω_m , Ω_b , h , n_s , and

⁷ <https://franciscovillaescusa.github.io/hades.html>

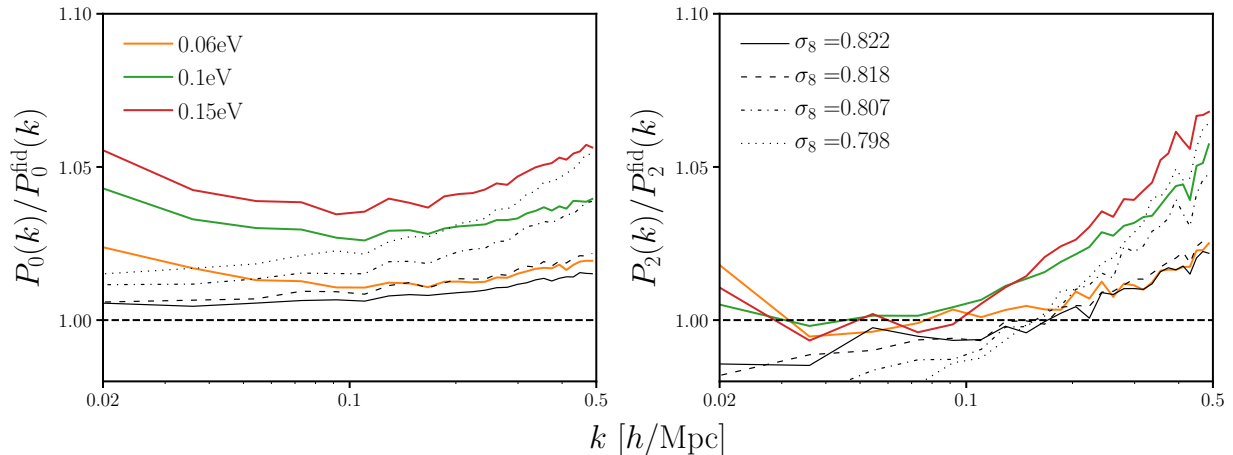


Figure 1. Impact of M_ν and σ_8 on the redshift-space halo power spectrum monopole and quadrupole measured using the HADES simulation suite. M_ν and σ_8 produce almost identical effects on halo clustering on small scales ($k > 0.1 h/\text{Mpc}$). This degeneracy can be partially broken through the quadrupole; however, M_ν and σ_8 produce almost the same effect on two-point clustering — within a few percent.

σ_8 , the fiducial cosmology is adjusted by either a small step above or below the fiducial value: $\{\Omega_m^+, \Omega_m^-, \Omega_b^+, \Omega_b^-, h^+, h^-, n_s^+, n_s^-, \sigma_8^+, \sigma_8^-\}$. Along M_ν , because $M_\nu \geq 0.0$ eV and the derivative of certain observable with respect to M_ν is noisy, Quijote includes sets of 500 simulations for $M_\nu = 0.1, 0.2$, and 0.4 eV. Table 1 lists the cosmologies included in the Quijote suite.

The initial conditions for all Quijote simulations were generated at $z = 127$ using 2LPT for simulations with massless neutrinos and the Zel’dovich approximation for massive neutrinos. Like HADES, the initial conditions of simulations with massive neutrinos take their scale-dependent growth factors/rates into account using the Zennaro et al. (2017) method. From the initial conditions, all of the simulations follow the gravitational evolution of 512^3 dark matter particles, and 512^3 neutrino particles (for massive neutrino models), to $z = 0$ using GADGET-III TreePM+SPH code (same as HADES). For further details on the Quijote simulations, we refer readers to Villaescusa-Navarro et al. (in preparation).

3. BISPECTRUM

We’re interested in breaking parameter degeneracies that limit the constraining power on M_ν of two-point clustering analyses using three-point clustering statistics — *i.e.* the bispectrum. In this section, we describe the bispectrum estimator used throughout the paper. We focus on the bispectrum monopole ($\ell = 0$) and use an estimator that exploits the speed of Fast Fourier Transforms (FFTs). Our estimator is similar to the estimators described in Scoccimarro (2015) and Sefusatti et al. (2016); we also follow their formalism in our description below. Although Sefusatti et al. (2016) and Scoccimarro (2015) respectively describe estimators in real- and redshift-space, since we focus on the bispectrum monopole, we note that there is no difference.

To measure the bispectrum of our halo catalogs, we begin by interpolating the halo positions to a grid, $\delta(\mathbf{x})$, and Fourier transforming the grid to get $\delta(\mathbf{k})$. We use a fourth-order interpolation to

Table 1. Specifications of the HADES and Quijote simulation suites.

| Name | M_ν (eV) | Ω_m | Ω_b | h | n_s | σ_8^m ($10^{10}h^{-1}M_\odot$) | σ_8^c ($10^{10}h^{-1}M_\odot$) | realizations |
|---------------|-----------------|---------------|--------------|---------------|---------------|--|--|--------------|
| HADES suite | | | | | | | | |
| Fiducial | 0.0 | 0.3175 | 0.049 | 0.6711 | 0.9624 | 0.833 | 0.833 | 100 |
| | 0.06 | 0.3175 | 0.049 | 0.6711 | 0.9624 | 0.819 | 0.822 | 100 |
| | 0.10 | 0.3175 | 0.049 | 0.6711 | 0.9624 | 0.809 | 0.815 | 100 |
| | 0.15 | 0.3175 | 0.049 | 0.6711 | 0.9624 | 0.798 | 0.806 | 100 |
| | 0.0 | 0.3175 | 0.049 | 0.6711 | 0.9624 | 0.822 | 0.822 | 100 |
| | 0.0 | 0.3175 | 0.049 | 0.6711 | 0.9624 | 0.818 | 0.818 | 100 |
| | 0.0 | 0.3175 | 0.049 | 0.6711 | 0.9624 | 0.807 | 0.807 | 100 |
| | 0.0 | 0.3175 | 0.049 | 0.6711 | 0.9624 | 0.798 | 0.798 | 100 |
| Quijote suite | | | | | | | | |
| Fiducial | 0.0 | 0.3175 | 0.049 | 0.6711 | 0.9624 | 0.834 | 0.834 | 15,000 |
| M_ν^+ | <u>0.1</u> | 0.3175 | 0.049 | 0.6711 | 0.9624 | 0.834 | 0.834 | 500 |
| M_ν^{++} | <u>0.2</u> | 0.3175 | 0.049 | 0.6711 | 0.9624 | 0.834 | 0.834 | 500 |
| M_ν^{+++} | <u>0.4</u> | 0.3175 | 0.049 | 0.6711 | 0.9624 | 0.834 | 0.834 | 500 |
| Ω_m^+ | 0.0 | <u>0.3275</u> | 0.049 | 0.6711 | 0.9624 | 0.834 | 0.834 | 500 |
| Ω_m^- | 0.0 | <u>0.3075</u> | 0.049 | 0.6711 | 0.9624 | 0.834 | 0.834 | 500 |
| Ω_b^+ | 0.0 | 0.3175 | <u>0.051</u> | 0.6711 | 0.9624 | 0.834 | 0.834 | 500 |
| Ω_b^- | 0.0 | 0.3175 | <u>0.047</u> | 0.6711 | 0.9624 | 0.834 | 0.834 | 500 |
| h^+ | 0.0 | 0.3175 | 0.049 | <u>0.6911</u> | 0.9624 | 0.834 | 0.834 | 500 |
| h^- | 0.0 | 0.3175 | 0.049 | <u>0.6511</u> | 0.9624 | 0.834 | 0.834 | 500 |
| n_s^+ | 0.0 | 0.3175 | 0.049 | 0.6711 | <u>0.9824</u> | 0.834 | 0.834 | 500 |
| n_s^- | 0.0 | 0.3175 | 0.049 | 0.6711 | <u>0.9424</u> | 0.834 | 0.834 | 500 |
| σ_8^+ | 0.0 | 0.3175 | 0.049 | 0.6711 | 0.9624 | <u>0.849</u> | <u>0.849</u> | 500 |
| σ_8^- | 0.0 | 0.3175 | 0.049 | 0.6711 | 0.9624 | <u>0.819</u> | <u>0.819</u> | 500 |

Top: The HADES suite includes sets of 100 N -body simulations with degenerate massive neutrinos of $M_\nu = 0.06, 0.10$, and 0.15 eV as well as sets of simulations with massless neutrino and $\sigma_8 = 0.822, 0.818, 0.807$, and 0.798 to examine the $M_\nu - \sigma_8$ degeneracy. **Bottom:** The Quijote suite includes 15,000 N -body simulations at the fiducial cosmology to accurately estimate the covariance matrices. It also includes sets of 500 paired fixed simulations at different cosmologies, where only one parameter is varied from the fiducial value (underlined), to estimate derivatives of observables along the cosmological parameters.

interlaced grids, which has advantageous anti-aliasing properties that allow unbiased measurements up to the Nyquist frequency (Hockney & Eastwood 1981; Sefusatti et al. 2016). Then using $\delta(\mathbf{k})$, we

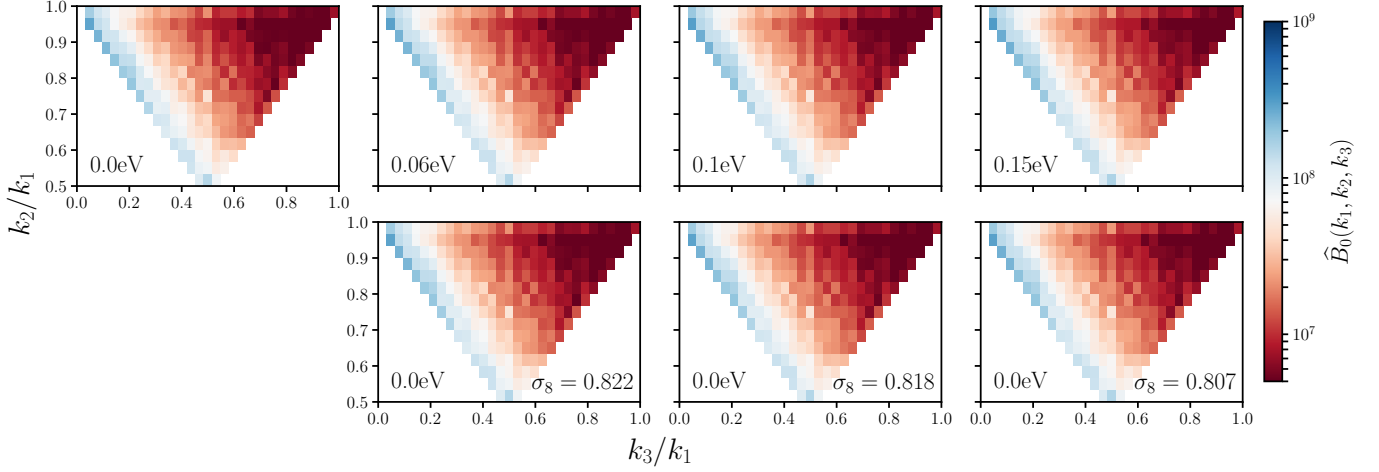


Figure 2. The redshift-space halo bispectrum, $\hat{B}_0(k_1, k_2, k_3)$, as a function of triangle configuration shape for $M_\nu = 0.0, 0.06, 0.10$, and 0.15 eV (upper panels) and $\sigma_8 = 0.822, 0.818$, and 0.807 (lower panels). The HADES simulations of the top and bottom panels in the three right-most columns, have matching σ_8 values (Section 2). We describe the triangle configuration shape by the ratio of the triangle sides: k_3/k_1 and k_2/k_1 . The upper left bin contains squeezed triangles ($k_1 = k_2 \gg k_3$); the upper right bin contains equilateral triangles ($k_1 = k_2 = k_3$); and the bottom center bin contains folded triangles ($k_1 = 2k_2 = 2k_3$). We include all triangle configurations with $k_1, k_2, k_3 \leq k_{\text{max}} = 0.5$ h/Mpc . and use the \hat{B}_0 estimator in Section 3.

measure the bispectrum monopole as

$$\hat{B}_{\ell=0}(k_1, k_2, k_3) = \frac{1}{V_B} \int_{k_1} d^3 q_1 \int_{k_2} d^3 q_2 \int_{k_3} d^3 q_3 \delta_D(\mathbf{q}_{123}) \delta(\mathbf{q}_1) \delta(\mathbf{q}_2) \delta(\mathbf{q}_3) - B_{\ell=0}^{\text{SN}}. \quad (1)$$

δ_D above is a Dirac delta function and hence $\delta_D(\mathbf{q}_{123}) = \delta_D(\mathbf{q}_1 + \mathbf{q}_2 + \mathbf{q}_3)$ ensures that the \mathbf{q}_i triplet actually form a closed triangle. Each of the integrals above represent an integral over a spherical shell in k -space with radius δk centered at \mathbf{k}_i :

$$\int_{k_i} d^3 q \equiv \int_{k_i - \delta k/2}^{k_i + \delta k/2} dq q^2 \int d\Omega. \quad (2)$$

V_B is a normalization factor proportional to the number of triplets \mathbf{q}_1 , \mathbf{q}_2 , and \mathbf{q}_3 that can be found in the triangle bin defined by k_1 , k_2 , and k_3 with width δk :

$$V_B = \int_{k_1} d^3 q_1 \int_{k_2} d^3 q_2 \int_{k_3} d^3 q_3 \delta_D(\mathbf{q}_{123}). \quad (3)$$

Lastly, $B_{\ell=0}^{\text{SN}}$ is the correction for the Poisson shot noise, which contributes due to the self-correlation of individual objects:

$$B_{\ell=0}^{\text{SN}}(k_1, k_2, k_3) = \frac{1}{\bar{n}} (P_0(k_1) + P_0(k_2) + P_0(k_3)) + \frac{1}{\bar{n}^2} \quad (4)$$

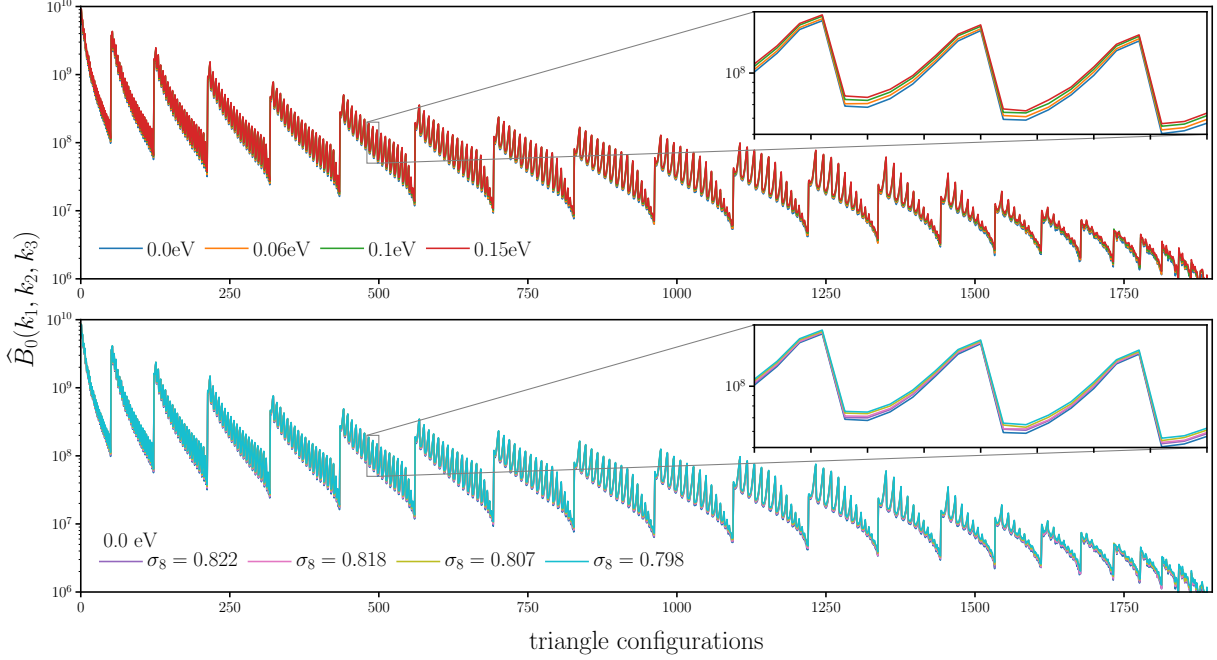


Figure 3. The redshift-space halo bispectrum, $\hat{B}_0(k_1, k_2, k_3)$, as a function of triangle configurations for $M_\nu = 0.0, 0.06, 0.10$, and 0.15 eV (top panel) and $M_\nu = 0.0$ eV, $\sigma_8 = 0.822, 0.818, 0.807$, and 0.798 (lower panel). We include all possible triangle configurations with $k_1, k_2, k_3 \leq k_{\text{max}} = 0.5$ h/Mpc where we order the configurations by looping through k_3 in the inner most loop and k_1 in the outer most loop satisfying $k_1 \leq k_2 \leq k_3$. In the insets of the panels we zoom into triangle configurations with $k_1 = 0.113$, $0.226 \leq k_2 \leq 0.283$, and $0.283 \leq k_3 \leq 0.377$ h/Mpc .

where \bar{n} is the number density of objects (halos) and P_0 is the powerspectrum monopole.

In order to evaluate the integrals in Eq. 1, we take advantage of the plane-wave representation of the Dirac delta function and rewrite the equation as

$$\hat{B}_{\ell=0}(k_1, k_2, k_3) = \frac{1}{V_B} \int \frac{d^3x}{(2\pi)^3} \int_{k_1} d^3q_1 \int_{k_2} d^3q_2 \int_{k_3} d^3q_3 \delta(\mathbf{q}_1) \delta(\mathbf{q}_2) \delta(\mathbf{q}_3) e^{i\mathbf{q}_{123} \cdot \mathbf{x}} - B_{\ell=0}^{\text{SN}} \quad (5)$$

$$= \frac{1}{V_B} \int \frac{d^3x}{(2\pi)^3} \prod_{i=1}^3 I_{k_i}(\mathbf{x}) - B_{\ell=0}^{\text{SN}} \quad (6)$$

where

$$I_{k_i}(\mathbf{x}) = \int_k d^3q \delta(\mathbf{q}) e^{i\mathbf{q} \cdot \mathbf{x}}. \quad (7)$$

At this point, we measure $\hat{B}_{\ell=0}(k_1, k_2, k_3)$ by calculating the I_{k_i} s with inverse FFTs and summing over in real space. For $\hat{B}_{\ell=0}$ measurements throughout the paper, we use $\delta(\mathbf{x})$ grids with $N_{\text{grid}} = 360$ and triangle configurations defined by k_1, k_2, k_3 bins of width $\Delta k = 3k_f = 0.01885$ h/Mpc , three times the fundamental mode $k_f = 2\pi/(1000$ $h^{-1}\text{Mpc})$ given the box size⁸.

⁸ The code that we use to evaluate $\hat{B}_{\ell=0}$ is publicly available at <https://github.com/changhoonhahn/pySpectrum>

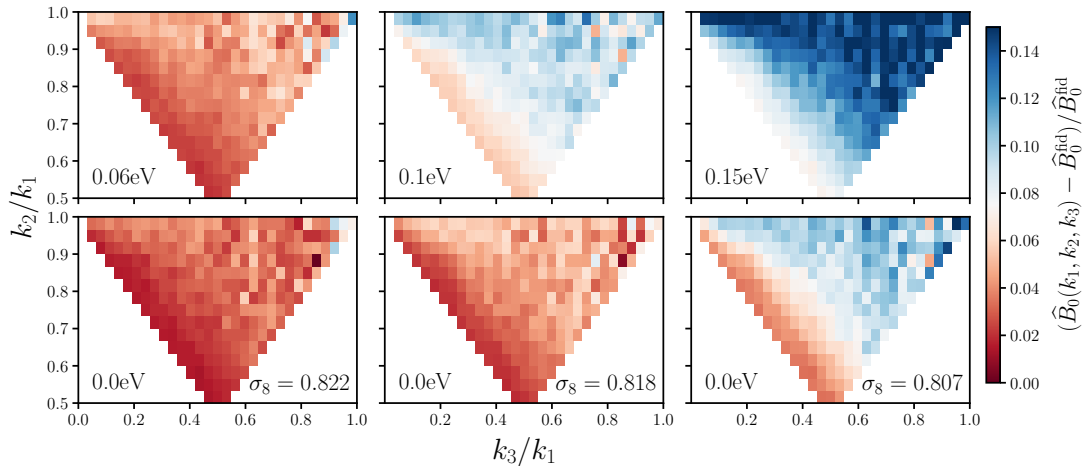


Figure 4. The shape dependence of the M_ν and σ_8 imprint on the redshift-space halo bispectrum, $\Delta\hat{B}_0/\hat{B}_0^{\text{fid}}$. We align the $M_\nu = 0.06, 0.10$, and 0.15 eV HADES models in the upper panels with $M_\nu = 0.0$ eV $\sigma_8 = 0.822, 0.818$, and 0.807 models on the bottom such that the top and bottom panels in each column have matching σ_8^c , which produce mostly degenerate imprints on the redshift-space power spectrum. The difference between the top and bottom panels highlight that M_ν leaves a distinct imprint on elongated and isosceles triangles (bins along the bottom left and bottom right edges, respectively) from σ_8 . *The imprint of M_ν has an overall distinct shape dependence on the bispectrum that cannot be replicated by varying σ_8 .*

We present the redshift-space halo bispectrum of the HADES simulations measured using the estimator above in two ways: one that emphasizes the triangle shape dependence (Figure 2) and the other that emphasizes the amplitude (Figure 3). In Figure 2, we plot $\hat{B}_0(k_1, k_2, k_3)$ as a function of k_2/k_1 and k_3/k_1 , which describe the triangle configuration shape. In each panel, the colormap of the $(k_2/k_1, k_3/k_1)$ bins represent the weighted average \hat{B}_0 amplitude of all triangle configurations in the bins. The upper left bins contain squeezed triangles ($k_1 = k_2 \gg k_3$); the upper right bins contain equilateral triangles ($k_1 = k_2 = k_3$); and the bottom center bins contain folded triangles ($k_1 = 2k_2 = 2k_3$). We include all possible 1898 triangle configurations with $k_1, k_2, k_3 < k_{\text{max}} = 0.5$ h/Mpc. The \hat{B}_0 in the upper panels are HADES models with $M_\nu = 0.0$ (fiducial), $0.06, 0.10$, and 0.15 eV; \hat{B}_0 in the lower panels are HADES models with $M_\nu = 0.0$ eV and $\sigma_8 = 0.822, 0.818$, and 0.807 . The top and bottom panels of the three right-most columns have matching σ_8 values (Section 2).

Next, in Figure 3, we plot $\hat{B}_0(k_1, k_2, k_3)$ for all possible triangle configurations with $k_1, k_2, k_3 < k_{\text{max}} = 0.5$ h/Mpc where we order the configurations by looping through k_3 in the inner most loop and k_1 in the outer most loop with $k_1 \leq k_2 \leq k_3$. In the top panel, we present \hat{B}_0 of HADES models with $M_\nu = 0.0, 0.06, 0.10$, and 0.15 eV; in the lower panel, we present \hat{B}_0 of HADES models with $M_\nu = 0.0$ eV and $\sigma_8 = 0.822, 0.818$, and 0.807 . We zoom into triangle configurations with $k_1 = 0.113$, $0.226 \leq k_2 \leq 0.283$, and $0.283 \leq k_3 \leq 0.377$ h/Mpc in the insets of the panels.

4. RESULTS

4.1. Breaking the $M_\nu - \sigma_8$ degeneracy

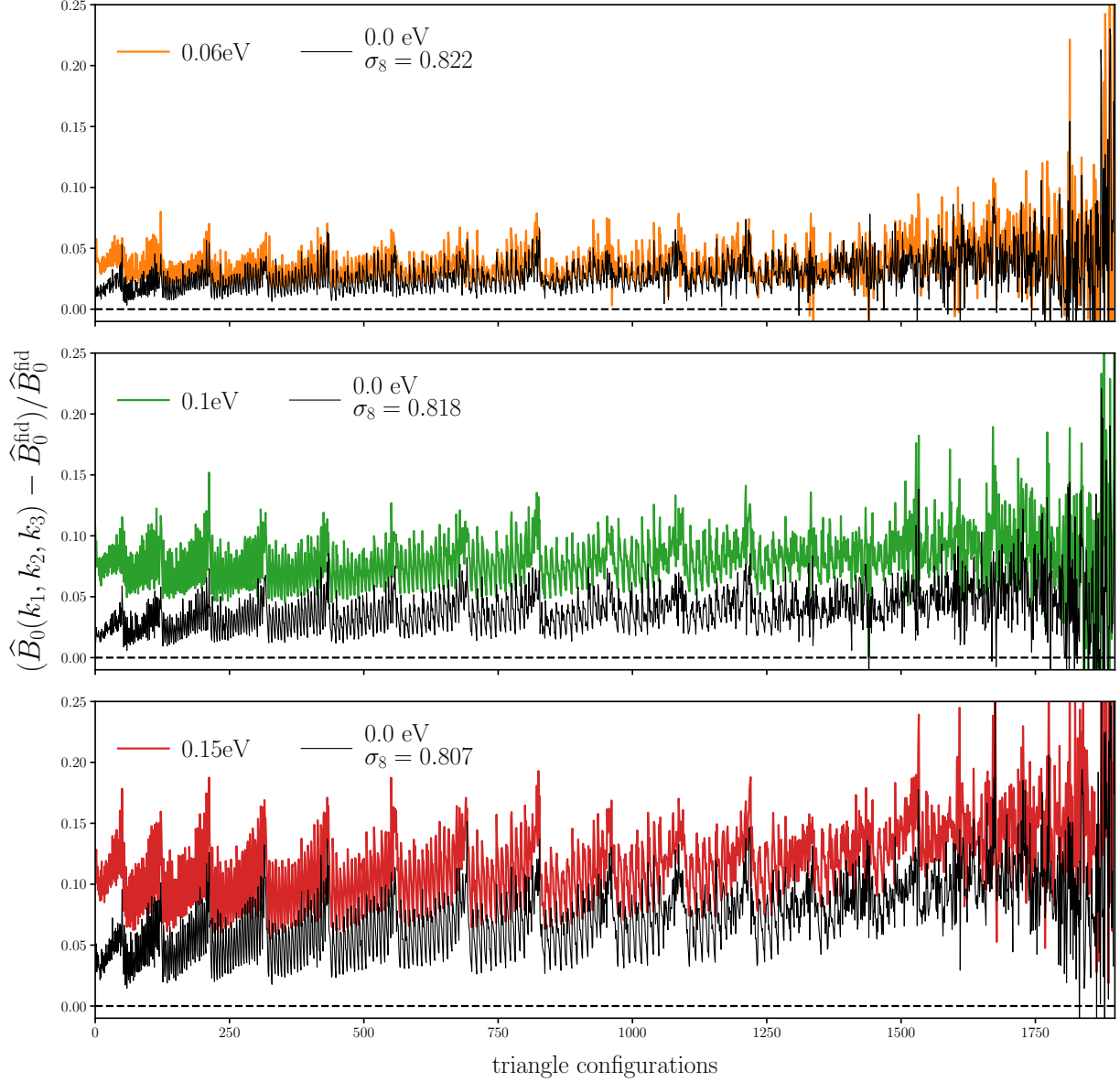


Figure 5. The impact of M_ν and σ_8 on the redshift-space halo bispectrum, $\Delta\hat{B}_0/\hat{B}_0^{\text{fid}}$, for all 1898 triangle configurations with $k_1, k_2, k_3 \leq 0.5h/\text{Mpc}$. We compare $\Delta\hat{B}_0/\hat{B}_0^{\text{fid}}$ of the $M_\nu = 0.06$ (top), 0.10 (middle), and 0.15 eV (bottom) HADES models to $\Delta\hat{B}_0/\hat{B}_0^{\text{fid}}$ of $M_\nu = 0.0$ eV $\sigma_8 = 0.822, 0.818$, and 0.807 models. The impact of M_ν on the bispectrum has a significantly different amplitude than the impact of σ_8 . For instance, $M_\nu = 0.15$ eV (red) has a $\sim 5\%$ stronger impact on the bispectrum than $M_\nu = 0.0$ eV $\sigma_8 = 0.798$ (black) even though their powerspectrums only differ by $< 1\%$ (Figure 1). Combined with the different shape-dependence (Figure 4), the distinct imprint of M_ν on the bispectrum illustrate that the bispectrum can break the degeneracy between M_ν and σ_8 that degrade constraints from two-point analyses.

One major bottleneck of constraining M_ν with the power spectrum alone is the strong $M_\nu - \sigma_8$ degeneracy. The imprint of M_ν and σ_8 on the power spectrum are degenerate and for models with the same σ_8^c , the power spectrum only differ by $< 1\%$ (see Figure 1 and Villaescusa-Navarro et al.

2018). The HADES suite, which has simulations with $M_\nu = 0.0, 0.06, 0.10$, and 0.15 eV as well as $M_\nu = 0.0$ eV simulations with matching σ_8^c , provides an ideal set of simulations to separate the impact of M_ν and examine the degeneracy between M_ν and σ_8 (Section 2 and Table 1). We measure the bispectrum of the HADES simulations (Figure 2 and 3), and present how the bispectrum can significantly improve M_ν constraints by breaking the $M_\nu - \sigma_8$ degeneracy.

We begin by examining the triangle shape dependent imprint of M_ν on the redshift-space halo bispectrum versus σ_8 alone. In Figure 4, we present the fractional residual, $(\Delta\hat{B}_0 = \hat{B}_0 - \hat{B}_0^{\text{fid}})/\hat{B}_0^{\text{fid}}$, as a function of k_2/k_1 and k_3/k_1 for $M_\nu = 0.06, 0.10$, and 0.15 eV in the upper panels and 0.0 eV $\sigma_8 = 0.822, 0.818$, and 0.807 in the bottom panels. The simulations in the top and bottom panels of each column have matching σ_8^c . Overall as M_ν increases, the bispectrum increases for all triangle shapes (top panels). This increase is due to halo bias (Villaescusa-Navarro et al. 2018, see also Figure 1). We impose a fixed M_{lim} on our halos so lower values of σ_8 translate to a larger halo bias, which boosts the amplitude of the bispectrum. Within the overall increase in amplitude, however, there is a significant triangle dependence. Equilateral triangles (upper left) have the largest increase. For $M_\nu = 0.15$ eV, the bispectrum is $\sim 15\%$ higher than \hat{B}_0^{fid} for equilateral triangles while only $\sim 8\%$ higher for folded triangles (lower center). The noticeable difference in $\Delta\hat{B}_0/\hat{B}_0^{\text{fid}}$ between equilateral and squeezed triangles (upper left) is roughly consistent with the comparison in Figure 7 of Ruggeri et al. (2018). They, however, fix A_s in their simulations and measure the real-space halo bispectrum so we refrain from any detailed comparisons.

As σ_8 increases with $M_\nu = 0.0$ eV, the bispectrum also increases overall for all triangle shapes (bottom panels). However, the comparison of the top and bottom panels in each column reveals significant differences in $\Delta\hat{B}_0/\hat{B}_0^{\text{fid}}$ for M_ν versus σ_8 alone. Between $M_\nu = 0.15$ eV and $\{0.0 \text{ eV}, \sigma_8 = 0.807\}$ cosmologies, there is an overall $\gtrsim 5\%$ difference in the bispectrum. In addition, the shape dependence of the $\Delta\hat{B}_0/\hat{B}_0^{\text{fid}}$ increase is different for M_ν than σ_8 . This is particularly clear in the differences between 0.1 eV (top center panel) and $\{0.0 \text{ eV}, \sigma_8 = 0.807\}$ (bottom right panel): near equilateral triangles in the two panels have similar $\Delta\hat{B}_0/\hat{B}_0^{\text{fid}}$ while triangle shapes near the lower left edge from the squeezed to folded triangles have significantly different $\Delta\hat{B}_0/\hat{B}_0^{\text{fid}}$. Hence, M_ν leaves an imprint on the bispectrum with a distinct triangle shape dependence than σ_8 alone. In other words, the triangle shape dependent imprint of M_ν on the bispectrum cannot be replicated by varying σ_8 — unlike the power spectrum.

We next examine the amplitude of the M_ν imprint on the redshift-space halo bispectrum versus σ_8 alone for all triangle configurations. We present $\Delta\hat{B}_0/\hat{B}_0^{\text{fid}}$ for all 1898 possible triangle configurations with $k_1, k_2, k_3 < k_{\text{max}} = 0.5 \text{ h/Mpc}$ in Figure 5. We compare $\Delta\hat{B}_0/\hat{B}_0^{\text{fid}}$ of the $M_\nu = 0.06, 0.10$, and 0.15 eV HADES models to the $\Delta\hat{B}_0/\hat{B}_0^{\text{fid}}$ of $M_\nu = 0.0$ eV $\sigma_8 = 0.822, 0.818$, and 0.807 models in the top, middle, and bottom panels, respectively. The comparison confirms the difference in overall amplitude of varying M_ν and σ_8 (Figure 4). For instance, $M_\nu = 0.15$ eV (red) has a $\sim 5\%$ stronger impact on the bispectrum than $M_\nu = 0.0$ eV $\sigma_8 = 0.798$ (black) even though their power spectra differ by $< 1\%$ (Figure 1).

The comparison in the panels of Figure 5 confirms the difference in the configuration dependence in $\Delta\hat{B}_0/\hat{B}_0^{\text{fid}}$ between M_ν versus σ_8 . The triangle configurations are ordered by looping through k_3

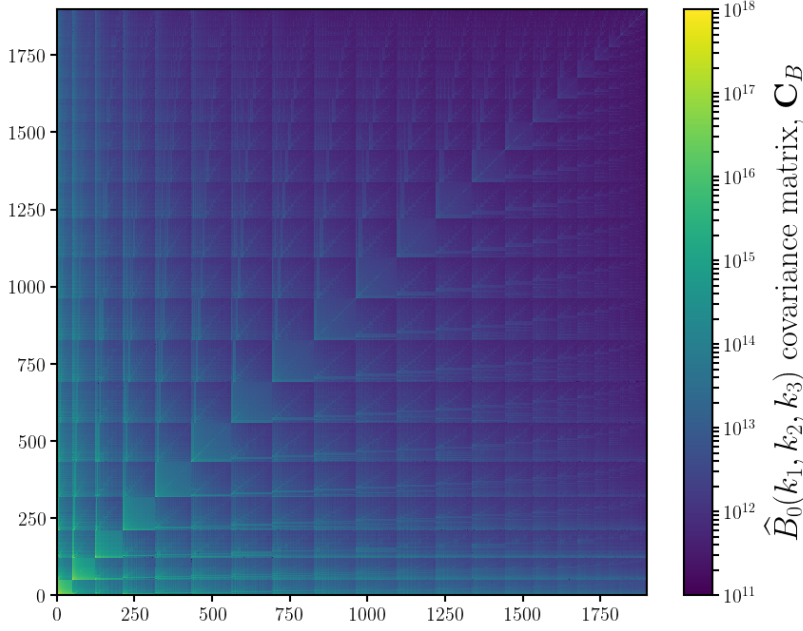


Figure 6. Covariance matrix of the redshift-space halo bispectrum estimated using $N_{\text{cov}} = 15,000$ realizations of the Quijote simulation suite at the fiducial cosmology: $\Omega_{\text{m}}=0.3175$, $\Omega_{\text{b}}=0.049$, $h=0.6711$, $n_s=0.9624$, $\sigma_8=0.834$, and $M_\nu=0.0$ eV. We include all possible triangle configurations with $k_1, k_2, k_3 \leq k_{\text{max}} = 0.5 h/\text{Mpc}$ and order the configurations (bins) in the same way as Figures 3 and 5. We use the covariance matrix above for the Fisher matrix forecasts presented in Section 4.2.

in the inner most loop and k_1 in the outer most loop such that $k_1 \leq k_2 \leq k_3$. In this ordering, k_1 increases from left to right. $\Delta\hat{B}_0/\hat{B}_0^{\text{fid}}$ of M_ν expectedly increases with k_1 : for small k_1 (on large scales), neutrinos behave like CDM and therefore the impact is reduced. However, $\Delta\hat{B}_0/\hat{B}_0^{\text{fid}}$ of M_ν has a smaller k_1 dependence than $\Delta\hat{B}_0/\hat{B}_0^{\text{fid}}$ of σ_8 . The distinct imprint of M_ν on the redshift-space halo bispectrum illustrates that the bispectrum can break the degeneracy between M_ν and σ_8 . Therefore, by including the bispectrum, we can more precisely constrain M_ν than with the power spectrum.

4.2. M_ν and other Cosmological Parameter Forecasts

We demonstrate in the previous section with the HADES simulations, that the bispectrum helps break the M_ν – σ_8 degeneracy, a major challenge in precisely constraining M_ν with the power spectrum. While this establishes the bispectrum as a promising probe for M_ν , we are ultimately interested in determining the constraining power of the bispectrum for an analysis that include cosmological parameters beyond M_ν and σ_8 —*i.e.* Ω_{m} , Ω_{b} , h , and n_s . The Quijote simulation suite is *specifically* designed to answer this question through Fisher matrix forecast.

First, the Quijote suite includes $N_{\text{cov}} = 15,000$ N -body realizations run at a fiducial cosmology: $M_\nu=0.0\text{eV}$, $\Omega_{\text{m}}=0.3175$, $\Omega_{\text{b}}=0.049$, $n_s=0.9624$, $h=0.6711$, and $\sigma_8=0.834$ (see Table 1). This allows us to robustly estimate the 1898×1898 covariance matrix of the bispectrum, \mathbf{C} (Figure 6). Second, the Quijote suite includes 500 N -body realizations evaluated at 13 different cosmologies, each a small step away from the fiducial cosmology parameter values along one parameter (Section 2 and Table 1).

We apply redshift-space distortions along 3 different directions for these 500 realizations, which then effectively gives us $N_{\text{deriv.}} = 1,500$ realizations. These simulations allow us to precisely estimate the derivatives of the bispectrum with respect to each of the cosmological parameters.

Since their introduction to cosmology over two decades ago, Fisher information matrices have been ubiquitously used to forecast the constraining power of future experiments (*e.g.* Jungman et al. 1996; Tegmark et al. 1997; Dodelson 2003; Heavens 2009; Verde 2010). Defined as

$$F_{ij} = - \left\langle \frac{\partial^2 \ln \mathcal{L}}{\partial \theta_i \partial \theta_j} \right\rangle, \quad (8)$$

where \mathcal{L} is the likelihood, the Fisher matrix for the bispectrum can be written as

$$F_{ij} = \frac{1}{2} \text{Tr} \left[\mathbf{C}^{-1} \frac{\partial \mathbf{C}}{\partial \theta_i} \mathbf{C}^{-1} \frac{\partial \mathbf{C}}{\partial \theta_j} + \mathbf{C}^{-1} \left(\frac{\partial \bar{B}_0}{\partial \theta_i} \frac{\partial \bar{B}_0}{\partial \theta_j}^T + \frac{\partial \bar{B}_0}{\partial \theta_i}^T \frac{\partial \bar{B}_0}{\partial \theta_j} \right) \right]. \quad (9)$$

Since we assume that the B_0 likelihood is Gaussian, including the first term in Eq. 9 runs the risk of incorrectly including information from the covariance already included in the mean (Carron 2013). We, therefore, conservatively neglect the first term and calculate the Fisher matrix as,

$$F_{ij} = \frac{1}{2} \text{Tr} \left[\mathbf{C}^{-1} \left(\frac{\partial \bar{B}_0}{\partial \theta_i} \frac{\partial \bar{B}_0}{\partial \theta_j}^T + \frac{\partial \bar{B}_0}{\partial \theta_i}^T \frac{\partial \bar{B}_0}{\partial \theta_j} \right) \right], \quad (10)$$

directly with \mathbf{C} and $\partial B_0 / \partial \theta_i$ along each cosmological parameter from the Quijote simulations.

For Ω_m , Ω_b , h , n_s , and σ_8 , we estimate

$$\frac{\partial \bar{B}_0}{\partial \theta_i} \approx \frac{\bar{B}_0(\theta_i^+) - \bar{B}_0(\theta_i^-)}{\theta_i^+ - \theta_i^-}, \quad (11)$$

where $\bar{B}_0(\theta_i^+)$ and $\bar{B}_0(\theta_i^-)$ are the average bispectrum of the 1,500 realizations at θ^+ and θ^- , respectively. Meanwhile, for M_ν , where the fiducial value is 0.0 eV and we cannot have negative M_ν , we use the Quijote simulations at M_ν^+ , M_ν^{++} , $M_\nu^{+++} = 0.1, 0.2, 0.4$ eV (Table 1) to estimate

$$\frac{\partial \bar{B}_0}{\partial M_\nu} \approx \frac{-21\bar{B}_0(M_\nu^{\text{fid}}) + 32\bar{B}_0(M_\nu^+) - 12\bar{B}_0(M_\nu^{++}) + \bar{B}_0(M_\nu^{+++})}{1.2}, \quad (12)$$

which provides a $\mathcal{O}(\delta M_\nu^2)$ order approximation. By using these N -body simulations, instead of analytic methods (*e.g.* perturbation theory), we exploit the accuracy of the simulations in the nonlinear regime and rely on fewer assumptions and approximations. In fact, these N -body simulation estimated derivatives are key in enabling us to quantify, for the first time, the full information content of the redshift-space bispectrum in the non-linear regime. We discuss subtleties of the bispectrum derivative and tests of convergence and stability in Appendix B.

We present the constraints on M_ν and other cosmological parameters $\{\Omega_m, \Omega_b, h, n_s, \sigma_8\}$ derived from the redshift-space halo bispectrum Fisher matrix for $k_{\text{max}} = 0.5 h/\text{Mpc}$ in Figure 7. We include Fisher constraints for the redshift-space halo power spectrum monopole with the same k_{max} for

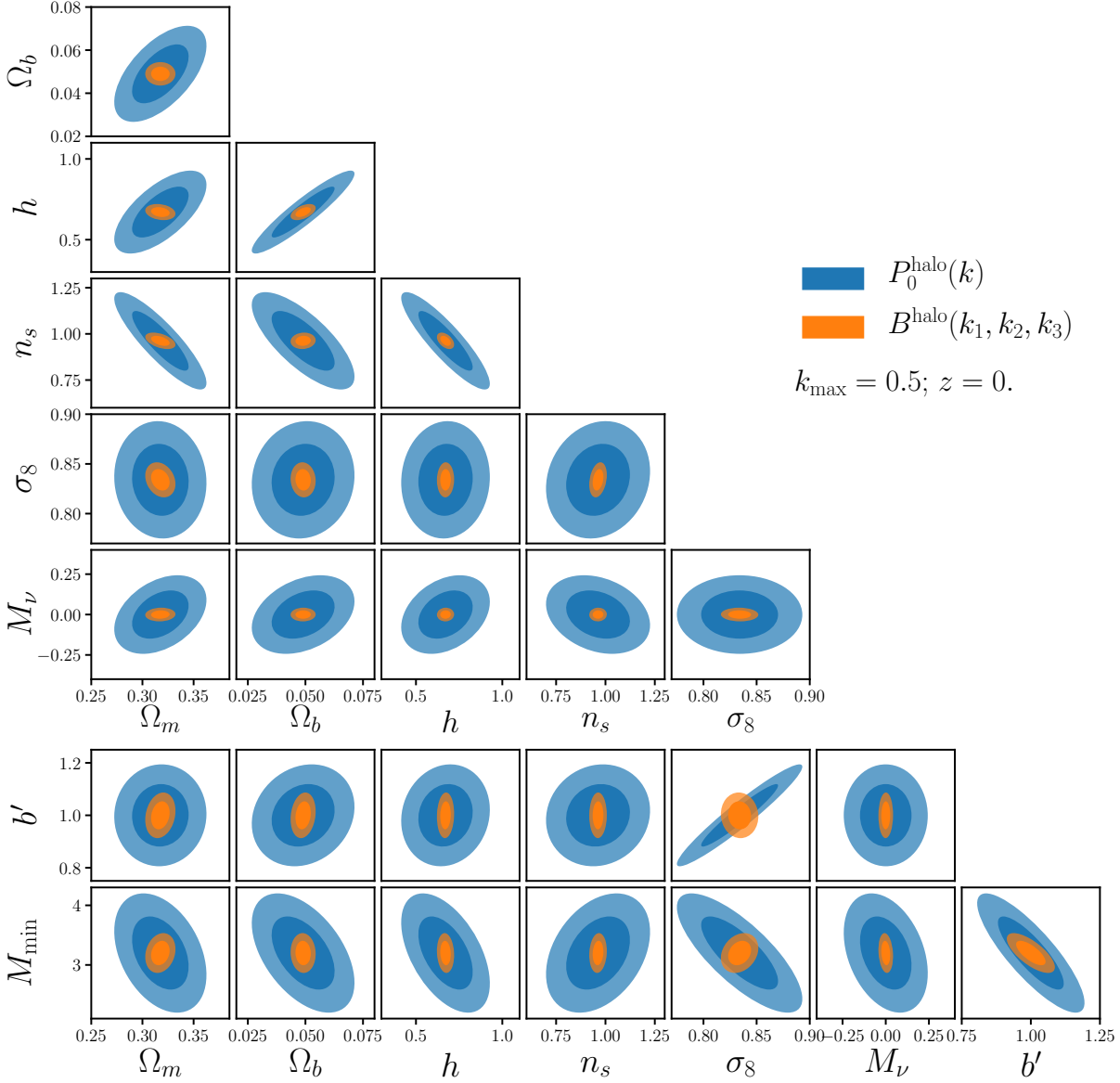


Figure 7. Fisher matrix constraints for M_ν and other cosmological parameters for the redshift-space halo bispectrum monopole (orange). We include Fisher parameter constraints for the redshift-space halo power-spectrum monopole in blue for comparison. The contours mark the 68% and 95% confidence intervals. We set $k_{\text{max}} = 0.5 \, h/\text{Mpc}$ for both power spectrum and bispectrum. We include in our forecasts b' and M_{\min} , a free amplitude scaling factor and halo mass limit, respectively. They serve as a simplistic bias model and we marginalize over them so that our constraints do not include extra constraining power from the difference in bias/number density in the different Quijote cosmologies. The bispectrum *substantially* improves constraints on all of the cosmological parameters over the power spectrum. Constraints on Ω_m , Ω_b , h , n_s , and σ_8 improve by factors of 3.1, 4.1, 5.1, 5.9, and 3.3, respectively. For M_ν , the bispectrum improves σ_{M_ν} from 0.1962 to 0.0342 eV — a factor of ~ 6 improvement over the power spectrum.

comparison (blue). The shaded contours mark the 68% and 95% confidence intervals. We include in our Fisher constraints the following nuisance parameters: b' and M_{\min} . b' is a scaling factor on the bispectrum amplitude, analogous to linear bias, and M_{\min} is the halo mass limit, which we choose as a nuisance parameter to address the difference in the number densities among the Quijote cosmologies, which impacts the derivatives $\partial\bar{B}_0/\partial\theta_i$. For instance, the σ_8^+ and σ_8^- cosmologies have halo $\bar{n} = 1.586 \times 10^{-4}$ and $1.528 \times 10^{-4}(h^{-1}\text{Mpc})^{-3}$. These parameters serve as a simplistic bias model and by marginalizing over them we aim to ensure that our Fisher constraints do not include extra constraining power from the difference in bias or number density. b' is a multiplicative factor so $\partial\bar{B}_0/\partial b' = \bar{B}_0$. $\partial\bar{B}_0/\partial M_{\min}$, we estimate numerically using \bar{B}_0 evaluated at $M_{\min}^+ = 3.3 \times 10^{13} h^{-1} M_\odot$ and $M_{\min}^- = 3.1 \times 10^{13} h^{-1} M_\odot$ with all other parameters set to the fiducial value.

The bispectrum substantially improves constraints on all parameters over the power spectrum. For $k_{\max} = 0.5 \text{ h/Mpc}$, the bispectrum tightens the marginalized 1σ constraints, σ_θ , of Ω_m , Ω_b , h , n_s , and σ_8 by factors of $\sim 3, 4, 5, 6$, and 3 over the power spectrum. *For M_ν , the bispectrum improves the constraint from $\sigma_{M_\nu} = 0.1962$ to 0.0342 eV — a factor of 6 improvement over the power spectrum.* This $\sigma_{M_\nu} = 0.0342 \text{ eV}$ constraint is for the *bispectrum alone* and only for a $1h^{-1}\text{Gpc}$ box. For a larger volume, V , σ_θ scales as $1/\sqrt{V}$. We list the precise marginalized Fisher parameter constraints of both cosmological and nuisance parameters for P_0 and B_0 in Table 2.

Even below $k_{\max} < 0.5 \text{ h/Mpc}$, the bispectrum significantly improves cosmological parameter constraints. We compare σ_θ of Ω_m , Ω_b , h , n_s , σ_8 , and M_ν as a function of k_{\max} for B_0 (orange) and P_0 (blue) in Figure 8. We only include the k_{\max} range where the Fisher forecast is well defined — *i.e.* more data bins than the number of parameters: $k_{\max} > 8 k_f \approx 0.05 \text{ h/Mpc}$ for P_0 and $k_{\max} > 12 k_f \approx 0.075 \text{ h/Mpc}$ for B_0 . Figure 8 reveals that the improvement of the bispectrum σ_θ over the power spectrum σ_θ is larger at higher k_{\max} . Although limited by the k_{\max} range, the figure suggests that on large scales ($k_{\max} \lesssim 0.1 \text{ h/Mpc}$) σ_θ of P_0 crosses over σ_θ of B_0 so P_0 has more constraining power than B_0 , as expected on linear scales. At slightly larger k_{\max} , $k_{\max} = 0.2 \text{ h/Mpc}$, we find that the bispectrum substantially improves σ_θ by factors of $\sim 1.8, 2.1, 2.6, 2.5, 2.6$, and 3.1 for Ω_m , Ω_b , h , n_s , σ_8 , and M_ν respectively.

Our forecasts demonstrate that the bispectrum has significant constraining power beyond the powerspectrum in the weakly nonlinear regime ($k > 0.1 \text{ h/Mpc}$). This constraining power comes from the bispectrum breaking degeneracies among the cosmological and nuisance parameters. This is evident when we compare the unmarginalized constraints from P_0 and B_0 : $1/\sqrt{F_{ii}}$ where F_{ii} is a diagonal element of the Fisher matrix. For $k < 0.4 \text{ h/Mpc}$, the unmarginalized constraints from P_0 are tighter than those from B_0 . Yet, once we marginalize the constraints over the other parameters, the B_0 constraints are tighter than P_0 for $k > 0.1 \text{ h/Mpc}$. The derivatives, $\partial B_0/\partial\theta_i$, also shed light on how B_0 breaks parameter degeneracies. The parameter degeneracies in the P_0 forecasts of Figure 7 are consistent with similarities in the shape and scale dependence of P_0 derivatives $\partial P_0/\partial\theta$. On the other hand, the B_0 derivatives with respect to the parameters have significant different scale and triangle shape dependences. **CH: derivative figure?**

By exploiting the massive number of N -body simulations of the Quijote suite, we present for the first time the full information content of the redshift-space bispectrum beyond the linear regime.

Table 2. Marginalized Fisher parameter constraints from the redshift-space halo power spectrum (top) and bispectrum (bottom) for different values of k_{max} . We list constraints for cosmological parameters M_ν , Ω_m , Ω_b , h , n_s , and σ_8 as well as nuisance parameters b' and M_{min}

| | k_{max} (h/Mpc) | M_ν (eV) | Ω_m | Ω_b | h | n_s | σ_8 | b' | M_{min} ($10^{13}h^{-1}M_\odot$) |
|-------|--|-------------------------------|-------------|-------------|-------------|-------------|-------------|-------------|--|
| | | 0.0 | 0.3175 | 0.049 | 0.6711 | 0.9624 | 0.834 | 1. | 3.2 |
| P_0 | 0.2 | ± 0.333 | ± 0.052 | ± 0.030 | ± 0.372 | ± 0.347 | ± 0.128 | ± 0.649 | ± 5.045 |
| | 0.3 | ± 0.277 | ± 0.044 | ± 0.023 | ± 0.273 | ± 0.276 | ± 0.069 | ± 0.383 | ± 2.457 |
| | 0.4 | ± 0.228 | ± 0.040 | ± 0.020 | ± 0.235 | ± 0.240 | ± 0.059 | ± 0.226 | ± 1.270 |
| | 0.5 | ± 0.196 | ± 0.036 | ± 0.018 | ± 0.207 | ± 0.213 | ± 0.048 | ± 0.157 | ± 0.807 |
| B_0 | 0.2 | ± 0.107 | ± 0.029 | ± 0.014 | ± 0.144 | ± 0.140 | ± 0.050 | ± 0.265 | ± 1.317 |
| | 0.3 | ± 0.065 | ± 0.020 | ± 0.008 | ± 0.077 | ± 0.074 | ± 0.023 | ± 0.143 | ± 0.657 |
| | 0.4 | ± 0.043 | ± 0.015 | ± 0.006 | ± 0.052 | ± 0.047 | ± 0.016 | ± 0.088 | ± 0.369 |
| | 0.5 | ± 0.034 | ± 0.012 | ± 0.004 | ± 0.040 | ± 0.036 | ± 0.014 | ± 0.070 | ± 0.269 |

The information content of the bispectrum has previously been examined using perturbation theory. Previous works, for instance, measure the signal-to-noise ratio (SNR) of the bispectrum derived from covariance matrices estimated using perturbation theory (Sefusatti & Scoccimarro 2005; Chan & Blot 2017). More recently, Chan & Blot (2017), used covariance matrices that include non-Gaussian contributions calibrated with N -body simulations to find that the cumulative SNR of the halo bispectrum is $\sim 30\%$ of the SNR of the halo power spectrum at $k_{\text{max}} \sim 0.1 h/\text{Mpc}$ and increases to $\sim 40\%$ at $k_{\text{max}} \sim 0.35 h/\text{Mpc}$. While these simple SNR measurements cannot be easily compared to Fisher analysis (), we note that they are roughly consistent with the unmarginalized constraints, which loosely represent the SNRs of the derivatives. Also, when we measure the halo power spectrum and bispectrum SNRs using our covariance matrices (Figure 6), we find a relation between the SNRs consistent with Chan & Blot (2017). Outside the k range explored by Chan & Blot (2017), $k_{\text{max}} > 0.35 h/\text{Mpc}$, we find that the SNR of B_0 continues to increase at higher k_{max} in contrast to the P_0 SNR, which saturates at $k_{\text{max}} \sim 0.1 h/\text{Mpc}$. At $k_{\text{max}} = 0.75 h/\text{Mpc}$, the largest k we measure the B_0 , the SNR of B_0 is $\sim 75\%$ of the SNR of P_0 .

Beyond these signal-to-noise calculations, a number of previous works have quantified the information content of the bispectrum with Fisher forecasts (Scoccimarro et al. 2004; Sefusatti et al. 2006; Sefusatti & Komatsu 2007; Song et al. 2015; Tellarini et al. 2016; Yamauchi et al. 2017; Karagiannis et al. 2018; Yankelevich & Porciani 2019). While most of these works fix most cosmological parameters and focus solely on forecasting constraints of primordial non-Gaussianity and bias parameters, Sefusatti et al. (2006) and Yankelevich & Porciani (2019) provide bispectrum forecasts for full sets of cosmological parameters. In Sefusatti et al. (2006), they present likelihood analysis forecasts for ω_d , ω_b , Ω_Λ , n_s , A_s , w , τ . For ΛCDM , with fixed bias parameters, and $k_{\text{max}} = 0.3 h/\text{Mpc}$, they find constraints on Ω_m , Ω_b , h , n_s , and σ_8 from WMAP, P_0 , and B_0 is ~ 1.5 times tighter than constraints

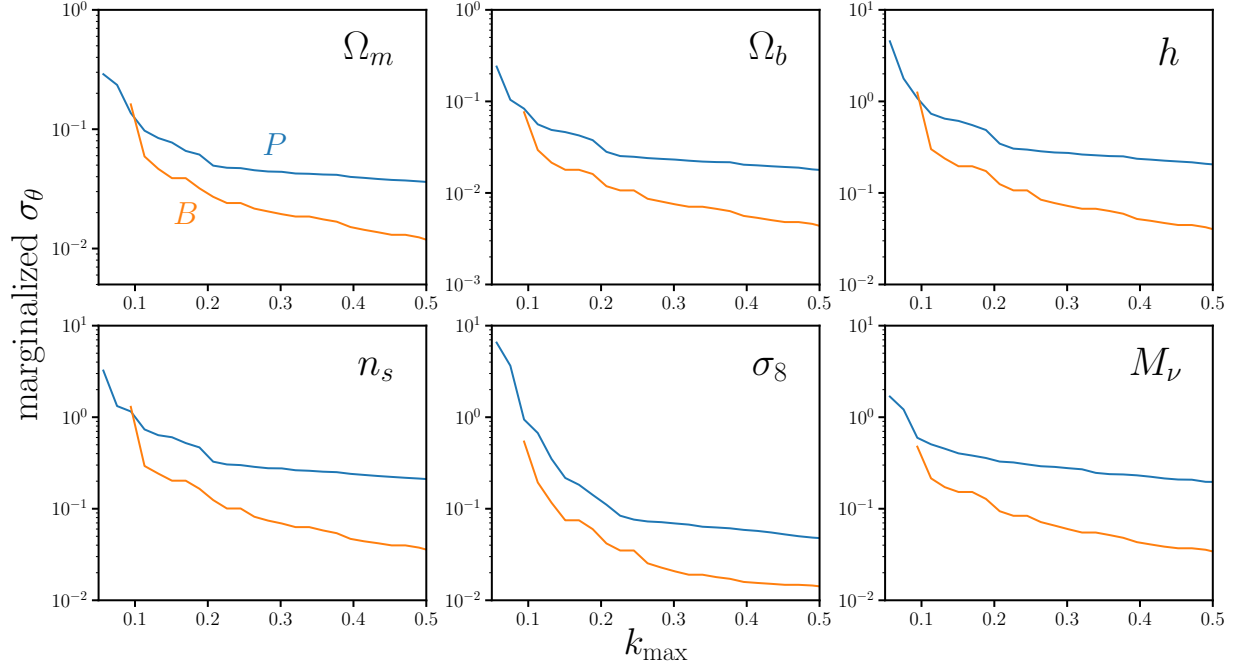


Figure 8. Marginalized 1σ constraints of the cosmological parameters Ω_m , Ω_b , h , n_s , σ_8 , and M_ν (σ_θ) as a function of k_{\max} for the redshift-space halo bispectrum (orange) and power spectrum (blue). Though not included in the figure, we marginalize over the nuisance parameters b' and M_{\min} in our forecast (Section 4.2). We only include $k_{\max} > 8k_f$ for P_0 and $k_{\max} > 12k_f$ for B_0 — k_{\max} ranges where we have more data bins than number of parameters. Even at $k_{\max} < 0.5$ h/Mpc , the bispectrum significantly improves cosmological parameter constraints. The improvement, however, is larger for higher k_{\max} . At $k_{\max} = 0.2$ h/Mpc , the bispectrum improves constraints on Ω_m , Ω_b , h , n_s , σ_8 , and M_ν by factors of ~ 1.8 , 2.1 , 2.6 , 2.5 , 2.6 , and 3.1 over the power spectrum.

from WMAP and P_0 . In comparison, for $k_{\max} = 0.3$ h/Mpc our B_0 constraints are tighter than P_0 constraints by factors of 2.1, 2.9, 3.5, 3.7, and 3.0. Both Sefusatti et al. (2006) and our analysis find significantly tighter constraints with the bispectrum. They however include the WMAP likelihood in their forecast and use perturbation theory models, which break down on small scales. In a comparison to N -body simulations, Lazanu et al. (2016) find that perturbation theory models of the matter bispectrum deviate by $> 5\%$ at $k_{\max} \gtrsim 0.15$ h/Mpc .

Yankelevich & Porciani (2019) present Fisher forecasts for Ω_{cdm} , Ω_b , h , n_s , A_s , w_0 , and w_0 for a Euclid-like survey (Laureijs et al. 2011) in 14 non-overlapping redshift bins over $0.65 < z < 2.05$. They use the full redshift-space bispectrum, rather than just the monopole, and a more sophisticated bias expansion than Sefusatti et al. (2006) but use a perturbation theory bispectrum model, which consequently limit their forecast to $k_{\max} = 0.15$ h/Mpc . They find similar constraining power on cosmological parameters from B alone as P . They also find that combining the bispectrum with the power spectrum only moderately improves parameter constraints because posterior correlations are similar for P and B . While this seemingly conflicts with the results we present, there are significant differences between our forecasts. For instance, their forecasts are at higher redshifts, $z > 0.7$, where

we expect the constraining power of B to be weaker than at $z = 0$. They also forecast the *galaxy* P and B and marginalizes over 56 nuisance parameters (14 z bins each with 3 bias parameters and 1 RSD parameter). They also neglect non-Gaussian contributions to the B covariance matrix, which substantially impact the constraints especially on small scales (Chan & Blot 2017). Despite differences, Yankelevich & Porciani (2019) find that the constraining power of B relative to P increases for higher k_{max} , consistent with our forecasts as a function of k_{max} (Figure 8). Also, consistent with their results, for $k_{\text{max}} = 0.15 \text{ h/Mpc}$, we find similar posterior correlations between the P_0 and B_0 constraints. At $k_{\text{max}} = 0.5 \text{ h/Mpc}$, however, we find the posterior correlations are no longer similar, which contribute to the constraining power of B_0 (Figure 7).

Various difference between our forecast and previous work prevent more thorough comparisons. Two crucial aspects, however, distinguish our forecasts from other works. We present the first bispectrum forecasts for a full set of cosmological parameters using bispectrum measured entirely from N -body simulations. This allows us to go beyond perturbation theory forecasts and quantify the full information content of the redshift-space bispectrum out to nonlinear regimes. Second, we present the first bispectrum forecast of cosmological parameters that includes neutrinos and demonstrates the constraining power of the bispectrum for M_ν . Below, we underline a few caveats of our forecasts.

Our forecasts are derived from Fisher matrices. Such forecasts make the assumption that the posterior is approximately Gaussian and, as a result, they underestimate the constraints for posteriors that are highly non-elliptical or asymmetric Wolz et al. (2012). Fisher matrices also rely on the stability, and in our case also convergence, of numerical derivatives. We examine the stability of the P_0 and B_0 derivatives with respect to M_ν by comparing the derivatives computed using N -body simulations at three different sets of cosmologies: (1) {fiducial, M_ν^+ , M_ν^{++} , and M_ν^{+++} } (Eq. 12), (2) {fiducial, M_ν^+ , and M_ν^{++} }, and (3) {fiducial and M_ν^+ } (see Appendix B; Figure 11). The derivatives computed using the different set of cosmologies, do not impact the Ω_m , Ω_b , h , n_s , and σ_8 constraints. They do however affect the M_ν constraints; but because P_0 and B_0 derivatives are affected by the same factor, the relative improvement of the $B_0 M_\nu$ constraint over the P_0 constraints is not impacted. In addition to the stability, because we use N -body simulations we test whether the convergence of our covariance matrix and derivatives impact our forecasts by varying the number of simulations used to estimate them: N_{cov} and N_{deriv} , respectively. For N_{cov} , we find $< 5\%$ variation in the Fisher matrix elements, $F_{i,j}$, for $N_{\text{cov}} > 5000$ and $< 1\%$ variation in σ_θ for $N_{\text{cov}} > 12000$. For N_{deriv} , we find $< 5\%$ variation in the $F_{i,j}$ elements and $< 5\%$ variation in σ_θ for $N_{\text{deriv}} > 1200$. Since our constraints vary by $< 10\%$ for sufficient N_{cov} and N_{deriv} , the convergence of the covariance matrix and derivatives do not impact our forecasts to the accuracy level of Fisher forecasting. We refer readers to Appendix B for a more details on the robustness of our results to the stability of the derivatives and convergence.

We argue that the constraining power of the bispectrum and its improvement over the power spectrum come from breaking degeneracies among the cosmological parameters. However, numerical noise can impact our forecasts when we invert the Fisher matrix. Since Planck constrain $\{\Omega_m, \Omega_b, h, n_s, \sigma_8\}$ tighter than the P_0 and B_0 alone (CH: @paco: citation to planck prior), the elements of the Planck prior matrix are larger than the elements of P_0 and B_0 Fisher matrices. Including Planck priors (*i.e.* adding the prior matrix to the Fisher matrix) increases the numerical stability of the

matrix inversion. It also reveals whether the bispectrum still improves parameter constraints once we include CMB constraints. With Planck priors and P_0 to $k_{\text{max}} = 0.5 \text{ h/Mpc}$, we derive the following constraints: $\sigma_{\Omega_m} = 0.0125$, $\sigma_{\Omega_b} = 0.0012$, $\sigma_h = 0.0086$, $\sigma_{n_s} = 0.0048$, and $\sigma_{\sigma_8} = 0.0194$. Including Planck priors expectedly tighten the constraints from P_0 alone. Meanwhile, with Planck priors and B_0 to $k_{\text{max}} = 0.5 \text{ h/Mpc}$, we get $\sigma_{\Omega_m} = 0.0086$, $\sigma_{\Omega_b} = 0.0008$, $\sigma_h = 0.0006$, $\sigma_{n_s} = 0.0043$, and $\sigma_{\sigma_8} = 0.0085$, 1.5, 1.6, 1.4, 1.1, and 2.3 times tighter constraints. For M_ν , $\sigma_{M_\nu} = 0.0802 \text{ eV}$ for P_0 and $\sigma_{M_\nu} = 0.0297 \text{ eV}$, a factor of 2.7 improvement. Since we find substantial improvements in parameter constraints with the Planck prior, the improvement from B_0 are numerically robust. Furthermore, σ_θ as a function of k_{max} with Planck priors reveal that while the constraining power of P_0 saturates at $k_{\text{max}} = 0.2 \text{ h/Mpc}$, the constraining power of B_0 continues to increase out to $k_{\text{max}} = 0.5 \text{ h/Mpc}$ (Figure 8),

Our forecasts are derived using the power spectrum and bispectrum in a *periodic box*. We do not consider a realistic geometry or radial selection function of actual observations from galaxy surveys. A realistic selection function will smooth out the triangle configuration dependence and consequently degrade the constraining power of the bispectrum. In Sefusatti & Scoccimarro (2005), for instance, they find that the signal-to-noise of the bispectrum is significantly reduced once survey geometry is included in their forecast. Survey geometry, however, also degrades the signal-to-noise of their power spectrum forecasts. Hence, with the substantial improvement in the M_ν constraints of the bispectrum, even with survey geometry we expect the bispectrum will significantly improve M_ν constraints over the power spectrum.

We include the nuisance parameter M_{min} in our forecasts to address the difference in halo bias and number densities among the Quijote cosmologies. Although we marginalize over M_{min} , this may not fully account for the extra information from \bar{n} and nonlinear bias leaking into the derivatives. To test this, we include extra nuisance parameters, $\{A_{\text{SN}}, B_{\text{SN}}, b_2, \gamma_2\}$, and examine their impact on our forecasts. A_{SN} and B_{SN} are multiplicative factors of the first and second terms of Eq. 4, which we include to account for any \bar{n} dependence that may be introduced from the shotnoise correction (Eq. 4). b_2 and γ_2 are the quadratic bias and nonlocal bias parameters (Chan et al. 2012; Sheth et al. 2013) to account for information from nonlinear bias. Marginalizing over b' , M_{min} , A_{SN} , B_{SN} , b_2 and γ_2 , we obtain the following constraints for B_0 with $k_{\text{max}} = 0.5 \text{ h/Mpc}$: $\sigma_{\Omega_m} = 0.0129$, $\sigma_{\Omega_b} = 0.0044$, $\sigma_h = 0.0404$, $\sigma_{n_s} = 0.0455$, $\sigma_{\sigma_8} = 0.0228$, and $\sigma_{M_\nu} = 0.0343$. While constraints on n_s and σ_8 are broadened from our fiducial forecasts, by 27% and 60%, the other parameters, especially M_ν , are not significantly impacted by marginalizing over the extra nuisance parameters. As another test, we calculate derivatives using halo catalogs from Quijote θ^- and θ^+ cosmologies with fixed \bar{n} . We similarly find no significant impact on the B_0 parameter constraints. Forecasts using additional nuisance parameters and with fixed \bar{n} derivatives, both support the robustness of our forecast. Yet these tests do not ensure that our forecast entirely marginalizes over halo bias.

In this paper, we focus on the halo bispectrum and power spectrum. However, constraints on M_ν will ultimately be derived from the distribution of galaxies. Besides the cosmological parameters, bias and nuisance parameters that allow us to marginalize over galaxy bias need to be incorporated to forecast M_ν and other cosmological parameter constraints for the galaxy bispectrum. Although we

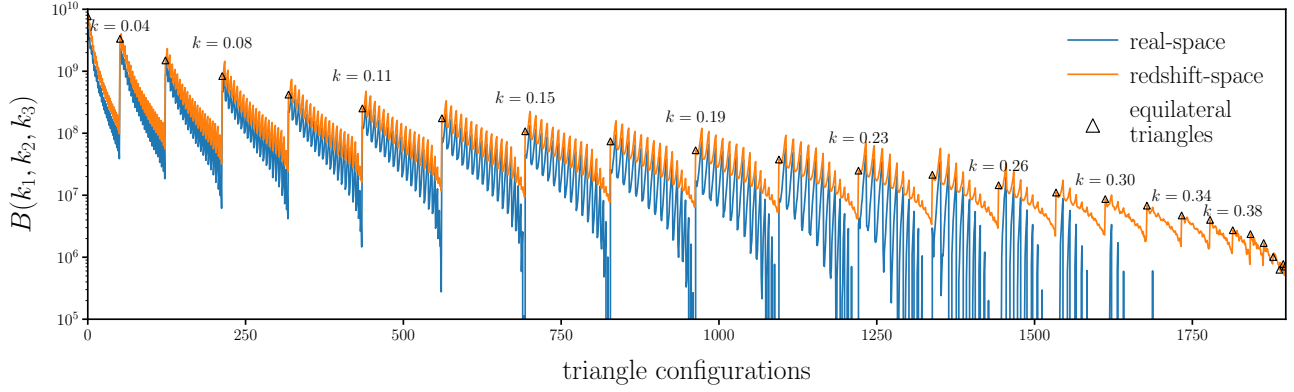


Figure 9. Comparison of the fiducial HADES simulations real and redshift-space halo bispectrum for triangle configurations with $k_1, k_2, k_3 \leq k_{\max} = 0.5h/\text{Mpc}$ (blue and orange respectively). We mark equilateral triangle configurations (empty triangle marker) along with their side lengths k .

include a *naive* bias model through b' and M_{\min} , and even b_2 and γ_2 in our tests, this is insufficient to describe how galaxies trace matter. A more realistic bias model such as a halo occupation distribution (HOD) model involve extra parameters that describe the distribution of central and satellite galaxies in halos (*e.g.* Zheng et al. 2005; Leauthaud et al. 2012; Tinker et al. 2013; Zentner et al. 2016; Vakili & Hahn 2019). We, therefore, refrain from a more exhaustive investigation of the impact of halo bias on our results and focus quantifying the constraining power of the galaxy bispectrum in the next paper of this series.

Marginalizing over galaxy bias parameters, will likely reduce the constraining power at high k . Hand et al. (2017), for instance, with their 13 parameter model only find a 15-30% improvement in $f\sigma_8$ when they extend their power spectrum multipole analysis from $0.2 h/\text{Mpc}$ to $0.4 h/\text{Mpc}$. However, jointly analyzing power spectrum and bispectrum will help break parameter degeneracies and improve constraints on cosmological parameters (Sefusatti et al. 2006; Yankelevich & Porciani 2019). We again emphasize that the constraints we present is for a $1h^{-1}\text{Gpc}$ box, a substantially smaller volume than upcoming surveys. Thus, even if the constraining power at high k is reduced, our forecasts suggest that the bispectrum offers significant improvements over the power spectrum, especially for constraining M_ν .

5. SUMMARY

CH: talk about DESI, PFS, WFIRST

ACKNOWLEDGEMENTS

It's a pleasure to thank Enea Di Dio, Daniel Eisenstein, Simone Ferraro, Shirley Ho, Emmaneul Schaan, Zachary Slepian, David N. Spergel, and Benjamin D. Wandelt for valuable discussions and comments.

APPENDIX

A. REDSHIFT-SPACE HALO BISPECTRUM

CH: do we want to keep this section?

B. FISHER FORECASTS USING N -BODY SIMULATIONS

The two key elements in calculating the Fisher matrices we use in our forecasts are the bispectrum covariance matrix (\mathbf{C} ; Figure 6) and the derivatives of the bispectrum along the cosmological and nuisance parameters, $\partial B_0/\partial\theta_i$ (Section 4.2). We compute both these elements directly using the N -body simulations of the Quijote suite (Section 2). This takes advantage of the N -body simulations and allows us to accurately quantify the constraining power of the bispectrum that come from the nonlinear regime. However, to trust our forecast, we must ensure that both \mathbf{C} has converged and that the numerically calculated $\partial B_0/\partial\theta_i$ do not introduce any biases. Below, we test the convergence of \mathbf{C} and $\partial B_0/\partial\theta_i$ and discuss some of the subtleties and caveats of numerically calculating $\partial B_0/\partial\theta_i$ from the Quijote simulations. CH: mention somewhere the P convergence looks good

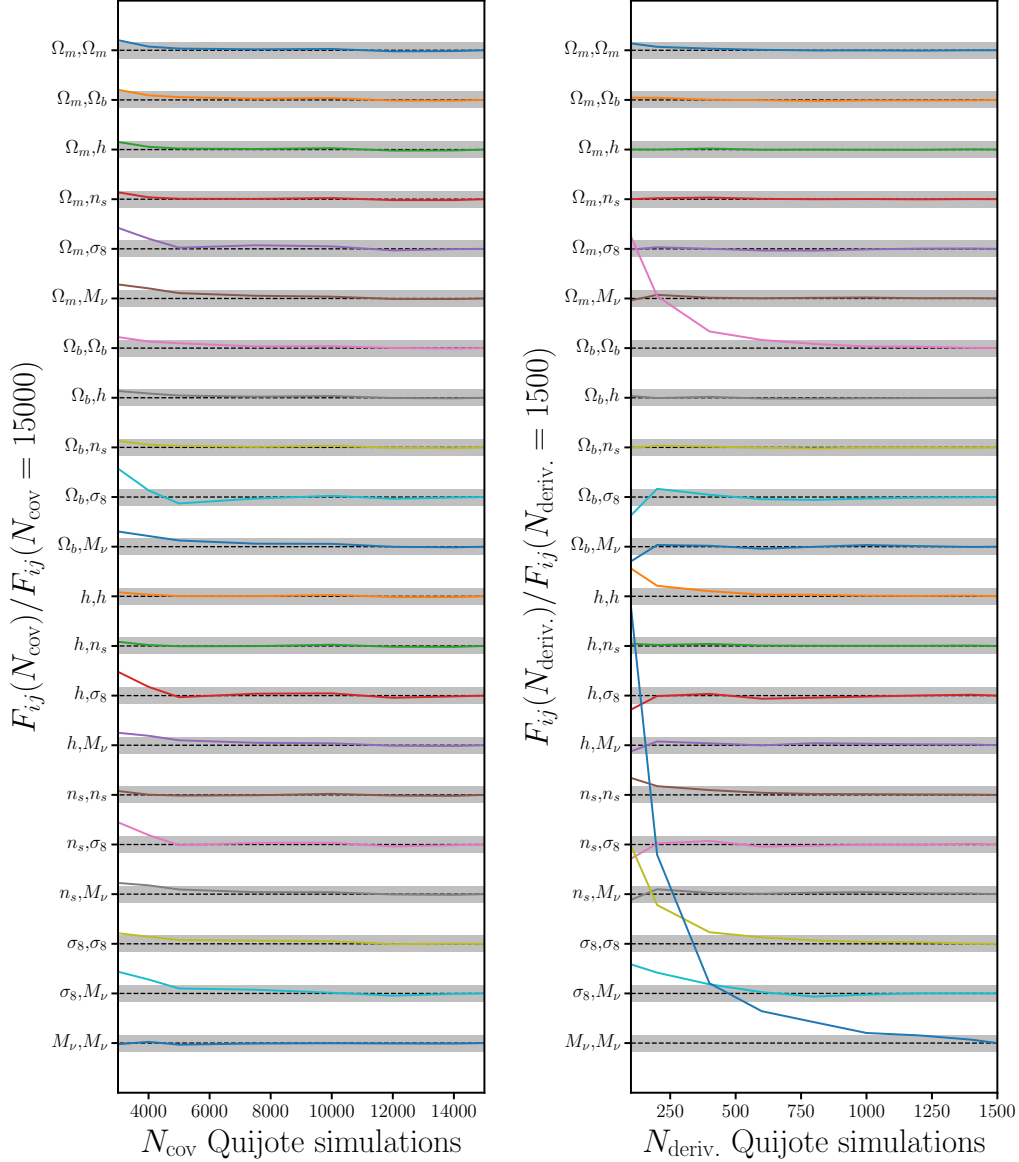
To estimate \mathbf{C} , we use 15,000 Quijote N -body simulations at the fiducial cosmology. This is a *significantly* larger number of simulations than previous bispectrum analyses; however, we also consider a larger number of triangle configurations — 1898 triangles out to $k_{\text{max}} = 0.5 \ h/\text{Mpc}$. For reference, the recent Gil-Marín et al. (2017) analysis used 2048 simulations to estimate the covariance matrix of the bispectrum with 825 configurations. We, therefore, check the convergence of \mathbf{C} by varying N_{fid} , the number of simulations used to estimate \mathbf{C} , and examining whether this significantly impacts the Fisher parameter constraints. We present $\sigma_\theta(N_{\text{fid}})/\sigma_\theta(N_{\text{fid}} = 15,000)$, the ratio of the 1σ Fisher constraint for $\theta = \Omega_m, \Omega_b, h, n_s, \sigma_8$, and M_ν calculated with N_{fid} over the constraint calculated with $N_{\text{fid}} = 15,000$, as a function of N_{fid} (Figure 10 left panel). The 1σ Fisher constraints on the parameters vary by $< 10\%$ for $N_{\text{fid}} > 7000$; in fact, the constraints vary by $< 1\%$ for $N_{\text{fid}} > 14,000$. Hence, we conclude that we have a sufficient number of simulations to estimate the bispectrum \mathbf{C} and our forecasts are robust to the convergence of \mathbf{C} .

We estimate $\partial B_0/\partial\theta_i$ numerically using 13 sets of $N_{\text{fp}} = 500$ fixed paired simulations (Table 1). To check the convergence of $\partial B_0/\partial\theta_i$ and its impact on our forecast we present the ratio of the 1σ Fisher constraint for θ calculated using N_{fp} simulations over the constraint calculated with $N_{\text{fp}} = 500$, $\sigma_\theta(N_{\text{fp}})/\sigma_\theta(N_{\text{fp}} = 500)$, as a function of N_{fp} (Figure 10 right panel). Unlike $\sigma_\theta(N_{\text{fid}})$, $\sigma_\theta(N_{\text{fp}})$ depend significantly on θ . For instance, σ_θ for σ_8 and Ω_m vary by $< 10\%$ for $N_{\text{fp}} > 300$ and $< 2\%$ for $N_{\text{fp}} > 450$. σ_θ for the other parameters vary significantly more. Nonetheless, for $N_{\text{fp}} > 400$ and 450 they vary by < 10 and 5% , respectively.

For $\Omega_m, \Omega_b, h, n_s, \sigma_8$, and M_{lim} we estimate $\partial B_0/\partial\theta_i$ using a centered difference approximation (Eq. 11). However, for M_ν , where we cannot have values below 0.0 eV, we cannot estimate the derivative with the same method. If we use the forward difference approximation,

$$\frac{\partial \overline{B}_0}{\partial M_\nu} \approx \frac{\overline{B}_0(M_\nu^{\text{fid}} + \delta M_\nu) - \overline{B}_0(M_\nu^{\text{fid}})}{\delta M_\nu}, \quad (\text{B1})$$

the error goes as $\mathcal{O}(\delta M_\nu)$. Instead, we use Eq. 12, which provides a $\mathcal{O}(\delta M_\nu^2)$ order approximation. In our $\partial B_0/\partial M_\nu$ approximation, we use the Quijote simulations at M_ν^+, M_ν^{++} , and M_ν^{+++} . We compare $\partial \log B(k_1, k_2, k_3)/\partial M_\nu$ (right) and $\partial \log P(k)/\partial M_\nu$ (left), computed using Eq. 12 (blue) and the forward difference approximation (green) in Figure 11. We also include P and B derivatives



approximated using only the M_ν^+ and M_ν^{++} simulations in orange. **CH: update numbers:** The three approximations for the derivatives differ from one another by roughly 10% with Eq. 12 producing the largest estimate for both P_0 and B_0 . If we use the M_ν^+ and M_ν^{++} and forward difference derivatives instead of the Eq. 12 for our Fisher forecasts, we find the following marginalized M_ν constraints for $k_{\text{max}} = 0.5 \text{ h/Mpc}$: 0.196 and 0.294eV for P_0 and 0.0308 and 0.0483eV for B_0 . These correspond to a ~ 20 and 80% relative increase from our forecasts in Section 4.2. The forward difference derivatives have a significant impact on our forecasts; however, we emphasize that this is a $\mathcal{O}(\delta M_\nu)$ approximation, unlike the other $\mathcal{O}(\delta M_\nu^2)$ approximations. Moreover, because the discrepancies in the derivative propagate similarly to the P_0 and B_0 constraints, the relative improvement of B_0 over P_0 remains roughly the same. Hence we conclude that the derivatives have sufficiently converged and robust for our Fisher forecasts.

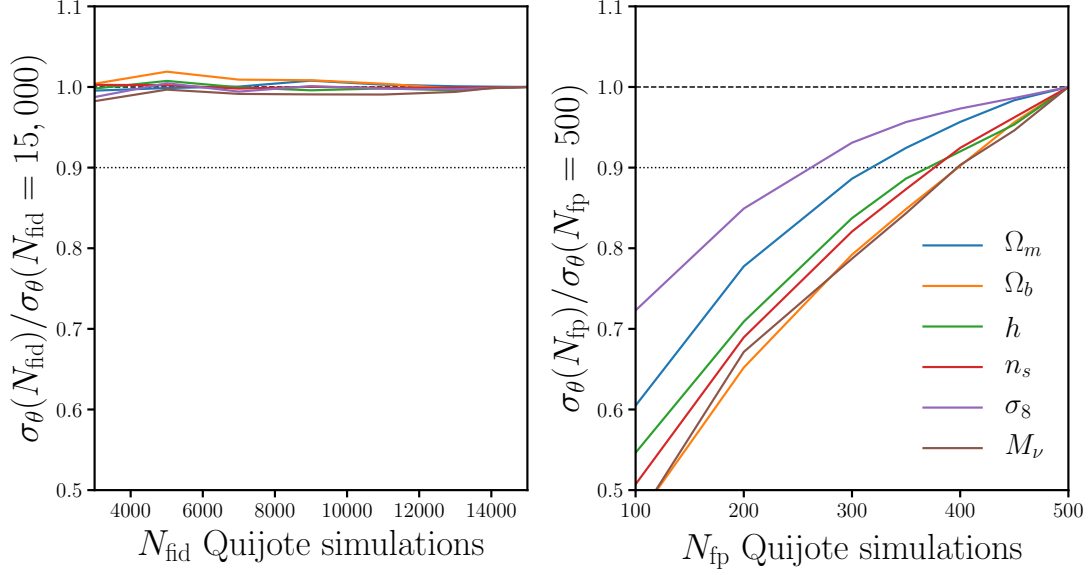


Figure 10. Left: The ratio of the 1σ Fisher constraint for $\theta = \Omega_m, \Omega_b, h, n_s, \sigma_8$, and M_ν calculated using N_{fid} Quijote simulations over the constraint calculated with all 15,000 simulations, $\sigma_\theta(N_{\text{fid}})/\sigma_\theta(N_{\text{fid}} = 15,000)$, as a function of N_{fid} . The N_{fid} simulations are used to estimate \mathbf{C} used to calculate the Fisher matrix (Eq. 10). The Fisher parameter constraints vary by < 10 and 1% for $N_{\text{fid}} > 7000$ and $14,000$, respectively. **Right:** The ratio of the 1σ Fisher constraint for θ calculated using N_{fp} simulations over the constraint calculated with all 500 fixed paired simulations, $\sigma_\theta(N_{\text{fp}})/\sigma_\theta(N_{\text{fp}} = 500)$, as a function of N_{fp} . The N_{fp} fixed paired simulations are used to numerically estimate $\partial B_0/\partial\theta_i$ in Eq. 10. Although $\sigma_\theta(N_{\text{fp}})/\sigma_\theta(N_{\text{fp}} = 500)$ vary among the parameters, for $N_{\text{fp}} > 400$ and 450 they vary by < 10 and 5% , respectively. Hence, *we have a sufficient number of simulations to estimate \mathbf{C} and the derivatives of the bipsectrum and our forecasts are robust to their convergence.*

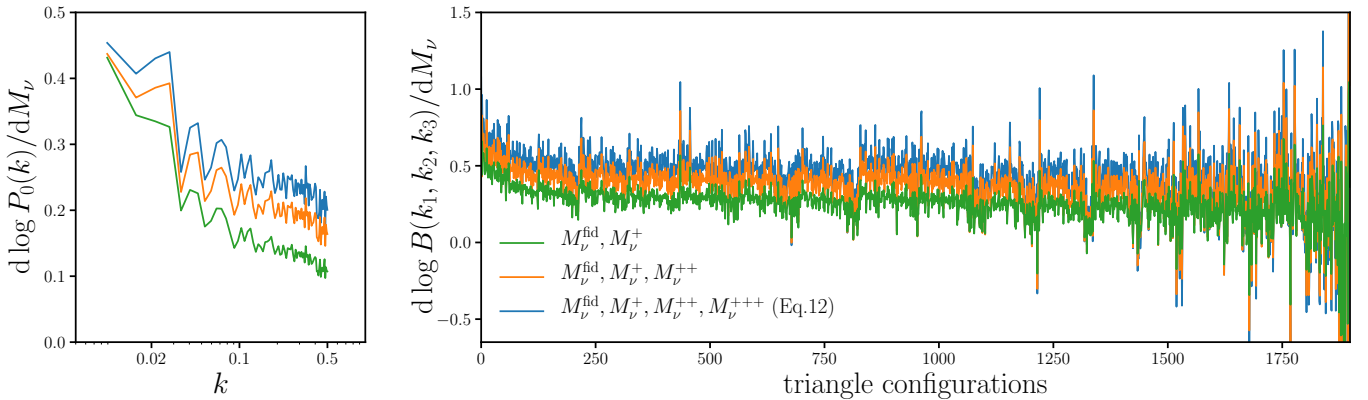


Figure 11. Comparison of $\partial \log B(k_1, k_2, k_3)/\partial M_\nu$ (right) and $\partial \log P(k)/\partial M_\nu$ (left), computed using Eq.12 (blue), excluding M_ν^{+++} (orange), and the forward difference approximation (green).

REFERENCES

- Abazajian, K. N., Adshead, P., Ahmed, Z., et al. 2016, [arXiv:1610.02743 \[astro-ph, physics:gr-qc, physics:hep-ph, physics:hep-th\]](#), [arXiv:1610.02743 \[astro-ph, physics:gr-qc, physics:hep-ph, physics:hep-th\]](#)
- Adamek, J., Durrer, R., & Kunz, M. 2017, [arXiv:1707.06938 \[astro-ph, physics:gr-qc\]](#), [arXiv:1707.06938 \[astro-ph, physics:gr-qc\]](#)
- Ade, P. a. R., Aghanim, N., Arnaud, M., et al. 2016, *Astronomy & Astrophysics*, **594**, [A13](#)
- Agarwal, S., & Feldman, H. A. 2011, *Monthly Notices of the Royal Astronomical Society*, **410**, [1647](#)
- Allison, R., Caucal, P., Calabrese, E., Dunkley, J., & Louis, T. 2015, *Physical Review D*, **92**, [123535](#)
- Archidiacono, M., Brinckmann, T., Lesgourgues, J., & Poulin, V. 2017, *Journal of Cosmology and Astro-Particle Physics*, **2017**, [052](#)
- Audren, B., Lesgourgues, J., Bird, S., Haehnelt, M. G., & Viel, M. 2013, *Journal of Cosmology and Astro-Particle Physics*, **2013**, [026](#)
- Boyle, A., & Komatsu, E. 2018, *Journal of Cosmology and Astro-Particle Physics*, **2018**, [035](#)
- Brandbyge, J., Hannestad, S., Haugbølle, T., & Thomsen, B. 2008, *Journal of Cosmology and Astro-Particle Physics*, **08**, [020](#)
- Carron, J. 2013, *Astronomy & Astrophysics*, **551**, [A88](#)
- Castorina, E., Carbone, C., Bel, J., Sefusatti, E., & Dolag, K. 2015, *Journal of Cosmology and Astro-Particle Physics*, **2015**, [043](#)
- Castorina, E., Sefusatti, E., Sheth, R. K., Villaescusa-Navarro, F., & Viel, M. 2014, *Journal of Cosmology and Astro-Particle Physics*, **02**, [049](#)
- Chan, K. C., & Blot, L. 2017, *Physical Review D*, **96**, [arXiv:1610.06585](#)
- Chan, K. C., Scoccimarro, R., & Sheth, R. K. 2012, *Physical Review D*, **85**, [083509](#)
- Collaboration, E., Knabenhans, M., Stadel, J., et al. 2018a, [arXiv:1809.04695 \[astro-ph\]](#), [arXiv:1809.04695 \[astro-ph\]](#)
- Collaboration, P., Aghanim, N., Akrami, Y., et al. 2018b, [arXiv:1807.06209 \[astro-ph\]](#), [arXiv:1807.06209 \[astro-ph\]](#)
- Davis, M., Efstathiou, G., Frenk, C. S., & White, S. D. M. 1985, *The Astrophysical Journal*, **292**, [371](#)
- Dodelson, S. 2003, *Modern Cosmology*
- Drexlin, G., Hannen, V., Mertens, S., & Weinheimer, C. 2013
- Emberson, J. D., Yu, H.-R., Inman, D., et al. 2017, *Research in Astronomy and Astrophysics*, **17**, [085](#)
- Font-Ribera, A., McDonald, P., Mostek, N., et al. 2014, *Journal of Cosmology and Astro-Particle Physics*, **05**, [023](#)
- Forero, D. V., Tórtola, M., & Valle, J. W. F. 2014, *Physical Review D*, **90**, [093006](#)
- Gerbino, M. 2018, [arXiv e-prints](#), [arXiv:1803.11545](#)
- Gil-Marín, H., Percival, W. J., Verde, L., et al. 2017, *Monthly Notices of the Royal Astronomical Society*, **465**, [1757](#)
- Gonzalez-Garcia, M. C., Maltoni, M., & Schwetz, T. 2016, *Nuclear Physics B*, **908**, [199](#)
- Hand, N., Seljak, U., Beutler, F., & Vlah, Z. 2017, [arXiv:1706.02362 \[astro-ph\]](#), [arXiv:1706.02362 \[astro-ph\]](#), [rEAD](#)
- Heavens, A. 2009, [arXiv:0906.0664 \[astro-ph\]](#), [arXiv:0906.0664 \[astro-ph\]](#)
- Heitmann, K., Higdon, D., White, M., et al. 2009, *The Astrophysical Journal*, **705**, [156](#)
- Hockney, R. W., & Eastwood, J. W. 1981, *Computer Simulation Using Particles*
- Ichiki, K., & Takada, M. 2012, *Physical Review D*, **85**, [063521](#)
- Jungman, G., Kamionkowski, M., Kosowsky, A., & Spergel, D. N. 1996, *Physical Review D*, **54**, [1332](#)
- Karagiannis, D., Lazanu, A., Liguori, M., et al. 2018, *Monthly Notices of the Royal Astronomical Society*, **478**, [1341](#)
- Kwan, J., Heitmann, K., Habib, S., et al. 2015, *The Astrophysical Journal*, **810**, [35](#)
- Laureijs, R., Amiaux, J., Arduini, S., et al. 2011, [arXiv e-prints](#), [arXiv:1110.3193](#)
- Lazanu, A., Giannantonio, T., Schmittfull, M., & Shellard, E. P. S. 2016, *Physical Review D*, **93**, [083517](#)
- Leauthaud, A., Tinker, J., Bundy, K., et al. 2012, *The Astrophysical Journal*, **744**, [159](#)
- Lesgourgues, J., & Pastor, S. 2012

- . 2014
- Liu, A., Pritchard, J. R., Allison, R., et al. 2016, *Physical Review D*, 93, 043013
- LoVerde, M. 2014, *Physical Review D*, 90, 083518
- Marulli, F., Carbone, C., Viel, M., Moscardini, L., & Cimatti, A. 2011, *Monthly Notices of the Royal Astronomical Society*, 418, 346
- McClintock, T., Rozo, E., Becker, M. R., et al. 2018, *arXiv:1804.05866 [astro-ph]*, *arXiv:1804.05866 [astro-ph]*
- Petracca, F., Marulli, F., Moscardini, L., et al. 2016, *Monthly Notices of the Royal Astronomical Society*, 462, 4208
- Ruggeri, R., Castorina, E., Carbone, C., & Sefusatti, E. 2018, *Journal of Cosmology and Astroparticle Physics*, 2018, 003
- Saito, S., Takada, M., & Taruya, A. 2008, *Physical Review Letters*, 100, 191301
- . 2009, *Physical Review D*, 80, 083528
- Sartoris, B., Biviano, A., Fedeli, C., et al. 2016, *Monthly Notices of the Royal Astronomical Society*, 459, 1764
- Scoccimarro, R. 2015, *Physical Review D*, 92, *arXiv:1506.02729*
- Scoccimarro, R., Sefusatti, E., & Zaldarriaga, M. 2004, *Physical Review D*, 69, 103513
- Sefusatti, E., Crocce, M., Pueblas, S., & Scoccimarro, R. 2006, *Physical Review D*, 74, *arXiv:astro-ph/0604505*
- Sefusatti, E., Crocce, M., Scoccimarro, R., & Couchman, H. M. P. 2016, *Monthly Notices of the Royal Astronomical Society*, 460, 3624
- Sefusatti, E., & Komatsu, E. 2007, *Physical Review D*, 76, 083004
- Sefusatti, E., & Scoccimarro, R. 2005, *Physical Review D*, 71, *arXiv:astro-ph/0412626*
- Sheth, R. K., Chan, K. C., & Scoccimarro, R. 2013, *Physical Review D*, 87, 083002
- Song, Y.-S., Taruya, A., & Oka, A. 2015, *Journal of Cosmology and Astro-Particle Physics*, 2015, 007
- Springel, V. 2005, *Monthly Notices of the Royal Astronomical Society*, 364, 1105
- Tegmark, M., Taylor, A. N., & Heavens, A. F. 1997, *The Astrophysical Journal*, 480, 22
- Tellarini, M., Ross, A. J., Tasinato, G., & Wands, D. 2016, *Journal of Cosmology and Astro-Particle Physics*, 2016, 014
- Tinker, J. L., Leauthaud, A., Bundy, K., et al. 2013, *The Astrophysical Journal*, 778, 93
- Upadhye, A., Kwan, J., Pope, A., et al. 2016, *Physical Review D*, 93, 063515
- Vakili, M., & Hahn, C. 2019, *The Astrophysical Journal*, 872, 115
- Verde, L. 2010, *arXiv:0911.3105 [astro-ph]*, 800, 147
- Viel, M., Haehnelt, M. G., & Springel, V. 2010, *Journal of Cosmology and Astro-Particle Physics*, 06, 015
- Villaescusa-Navarro, F., Banerjee, A., Dalal, N., et al. 2018, *The Astrophysical Journal*, 861, 53
- Villaescusa-Navarro, F., Bird, S., Peña-Garay, C., & Viel, M. 2013, *Journal of Cosmology and Astro-Particle Physics*, 2013, 019
- Villaescusa-Navarro, F., Marulli, F., Viel, M., et al. 2014, *Journal of Cosmology and Astro-Particle Physics*, 03, 011
- Wibking, B. D., Salcedo, A. N., Weinberg, D. H., et al. 2019, *Monthly Notices of the Royal Astronomical Society*, 484, 989
- Wolz, L., Kilbinger, M., Weller, J., & Giannantonio, T. 2012, *Journal of Cosmology and Astroparticle Physics*, 2012, 009
- Wong, Y. Y. Y. 2008, *Journal of Cosmology and Astroparticle Physics*, 2008, 035
- Yamauchi, D., Yokoyama, S., & Takahashi, K. 2017, *Physical Review D*, 95, 063530
- Yankelevich, V., & Porciani, C. 2019, *Monthly Notices of the Royal Astronomical Society*, 483, 2078
- Zennaro, M., Bel, J., Villaescusa-Navarro, F., et al. 2017, *Monthly Notices of the Royal Astronomical Society*, 466, 3244
- Zentner, A. R., Hearin, A., van den Bosch, F. C., Lange, J. U., & Villarreal, A. 2016, *arXiv:1606.07817 [astro-ph]*, *arXiv:1606.07817 [astro-ph]*
- Zhai, Z., Tinker, J. L., Becker, M. R., et al. 2018, *arXiv:1804.05867 [astro-ph]*, *arXiv:1804.05867 [astro-ph]*
- Zheng, Z., Berlind, A. A., Weinberg, D. H., et al. 2005, *The Astrophysical Journal*, 633, 791